

Cosmic ray validation of electrode positions in small-strip thin gap chambers for the upgrade of the ATLAS detector

Lia Formenti

Department of Physics
McGill University, Montreal
October, 2021

A thesis submitted to
McGill University
in partial fulfillment of the
requirements of the degree of
Master of Science

© Lia Formenti 2021

Table of Contents

1	Introduction	1
2	High energy particle physics	4
2.1	The Standard Model	4
2.2	Beyond the Standard Model	6
2.3	Studying high energy particle physics with accelerators	7
3	The LHC and the ATLAS experiment	9
3.1	The Large Hadron Collider	9
3.2	The High-Luminosity LHC	10
3.3	The ATLAS experiment	12
4	The New Small Wheels	18
4.1	Motivation for the New Small Wheels	18
4.2	Design of the NSWs	21
4.3	Small-strip thin gap chambers	21
4.4	sTGC Quadruplet Construction	23
4.5	NSW alignment	26
5	Using cosmic muons to measure relative strip position offsets	29
5.1	Cosmic rays	29
5.2	Experimental setup	30

5.3	Data acquisition	31
5.4	Data preparation	32
5.4.1	Data quality cuts on electrode hits	32
5.4.2	Clustering and tracking	32
5.5	Relative local offsets	34
5.6	Systematic uncertainty	40
5.7	Discussion	42
6	Using x-rays to measure relative strip position offsets	43
6.1	Experimental setup	43
6.2	Data acquisition	45
6.3	Data preparation	45
6.4	Measuring local offsets	45
6.5	Measuring relative local offsets	47
7	Comparing cosmic muon and x-ray relative strip position offsets	50
7.1	Results	50
7.2	Discussion	55
7.3	Next steps	56
8	Summary and outlook	58
References		59
APPENDICES		67
A	Cluster position uncertainty	68
B	Analysis statistics	70

C Analysis systematics	72
C.1 Residual distribution fit function	72
C.2 Cosmic muon data collection voltage	75
C.3 Cluster fit algorithm	76
C.4 Differential non-linearity	77
D Printable plots	80

Abstract

The Large Hadron Collider (LHC) is used to generate subatomic physics processes at the energy frontier to challenge our understanding of the Standard Model of particle physics. The particle collision rate at the LHC will be increased up to seven times its design value in 2025-2027 by an extensive upgrade program. The innermost endcaps of the ATLAS muon spectrometer consist of two wheels of muon detectors that must be replaced to maintain the muon momentum resolution in the high-rate environment. The so-called New Small Wheels (NSWs) are made of two detector technologies: micromegas and small-strip thin gap chambers (sTGCs). The sTGCs are gas ionization chambers that hold a thin volume of gas between two cathode boards. One board is segmented into copper readout strips of 3.2 mm pitch that are used to precisely reconstruct the coordinate of a passing muon. Modules of four sTGCs glued together into quadruplets cover the NSWs. Quadruplets were designed to achieve a 1 mrad angular resolution to fulfill the spectrometer's triggering and precision tracking requirements. To achieve the required angular resolution the absolute position of the readout strips must be known in the ATLAS coordinate system to within 100 μm . At McGill University, the performance of sTGC quadruplets was characterized using cosmic ray data before being sent to CERN, where the charge profile left by x-rays is used to measure the offset of the strip patterns with respect to nominal at a limited number of points on the surface of each quadruplet. The x-ray strip position measurements have acceptable but limited precision and do not span the whole area of the strip layers. Given the importance of knowing the absolute position of each readout strip to achieve the performance requirements of the NSWs, the x-ray method must be validated by an independent method. Cosmic ray data is used to characterize the relative alignment between layers and validate the x-ray method.

Résumé

Le grand collisionneur des hadrons (LHC) utilise des collisions de protons afin de générer des processus de la physique subatomique à la frontière même de la haute énergie, et ceci afin de tenter remettre en cause le modèle standard de la physique des particules. Le taux des collisions entre protons au LHC sera augmenté jusqu'à sept fois le taux nominal d'ici 2025-2027 à l'aide d'un programme de mise à niveau de grande envergure. Une partie du spectromètre à muons du détecteur ATLAS consistant de deux roues de détecteurs de muons doit être remplacée afin de maintenir la résolution sur l'inertie des muons à haut taux de collision. Appelées les Nouvelles Petites Roues (NSWs), elles utilisent deux technologies de détection différentes: des chambres micromegas et des chambres à petites bandes et à intervalles fins (sTGCs). Les sTGCs sont des chambres d'ionisation de gaz, qui contiennent un volume très fin de gaz entre deux panneaux cathodiques. Un panneau est segmenté avec de petites bandes en cuivre en pente de 3.2 mm. Ceux-ci détectent le signal laissé par des muons et permettent la mesure précise des coordonnées spatiales des muons qui traversent le détecteur. Des modules de quatre sTGCs collés ensemble en quadruplets couvrent la superficie des NSWs. Ces quadruplets ont été conçus afin de permettre une résolution angulaire de 1 mrad, et de satisfaire les exigences des systèmes de déclenchement et de mesures de précision. Afin d'atteindre cette résolution angulaire il faut que la position absolue de chaque bande soit connue au sein du détecteur ATLAS avec une précision d'au moins 100 μm . À l'Université de McGill, la performance des quadruplets a été caractériser avec des rayons cosmiques avant leur envoi au CERN, où le profil des charges laissé par des rayons X est utilisé pour mesurer le déplacement du motif des bandes par rapport à leur emplacement nominal. Ceci est fait à un nombre de positions limité sur la surface des quadruplets. Ces déplacements, mesurés par les rayons X, ont une précision acceptable mais limitée et ne couvrent pas la région entière des panneaux. Étant donné l'importance de la caractérisation précise de la position absolue de chaque bande afin de réaliser les exigences de rendement des NSWs, une méthode indépendante de validation de la méthode des rayons X est requise. Les données recueillies avec les rayons cosmiques sont utilisées pour caractériser l'alignement relatif entre les panneaux et valider la méthode des rayons X.

Acknowledgements

Experimental particle physics projects are never done alone. I am grateful to have been working with the ATLAS Collaboration for two years now.

Thank you to Dr. Brigitte Vachon for her guidance throughout this project and for editing this thesis. I am consistently amazed by her ability to jump into the details of my project and discuss them with me. She has also supported me as a whole person, encouraging me to pursue volunteering for science outreach and consider opportunities I may not have found on my own.

Thanks also to Dr. Benoit Lefebvre, who collected some of the data used in this thesis, wrote several software tools I used to analyze the data and advised me several times throughout this project.

Thank you to my labmates at McGill University, Dr. Tony Kwan, Kathrin Brunner, John McGowan and Charlie Chen. Kathrin taught me mechanical skills that I had not learned otherwise and that I will apply elsewhere. She also is my model of a thoughtful, careful and organized experimentalist. Tony, manager of the laboratory, created the most encouraging, trusting and productive work environment I have ever been a part of.

Thank you to the friends I can call on at anytime, and thank you to my family whose constant support makes every step possible.

Contribution of authors

I, the author, was involved in collecting the cosmic ray data from September 2019 - March 2021. I did not design the cosmic ray testing procedure nor write the data preparation software, but I participated in using the software to analyze cosmic ray results. In the thesis, the terms “clustering,” “local offset” and “relative local offset” are defined. Cosmic ray clustering was done in the data preparation software, but I redid the fit afterwards to explore sensitivity to the fit algorithm. With help from Dr. Lefebvre and Dr. Vachon, I helped design the software that calculated the relative local offsets from cosmic ray data. I wrote that software on my own. I was not involved in the design, data collection, data preparation or analysis of the x-ray data. I also was not involved in creating an alignment model from the x-ray data. I used the x-ray local offsets calculated using x-ray data analysis software to calculate relative local offsets with x-rays. I did the comparison between the x-ray and cosmic ray data.

I hereby declare that I am the sole author of this thesis. This is a true copy of the thesis, including any required final revisions, as accepted by my examiners.

Chapter 1

Introduction

The Standard Model (SM) is a theoretical framework that describes experimental observations of particles and their interactions at the smallest distance scales; however, the questions the SM does not address motivate more experimentation.

Accelerators collide particles to generate interactions that can be recorded by detectors for further study. Detectors measure the trajectory and energy of all secondary particles produced in collisions to understand the interaction. The Large Hadron Collider (LHC) [1] at CERN is the world's most energetic particle accelerator. Its energy makes it a unique tool to study elementary particles and their interactions in an environment with conditions similar to what would have existed in the early universe. If study at the energy frontier is to continue, the LHC must go on.

After 2025, the statistical gain in running the LHC further without significant increase in beam intensity will become marginal. The High Luminosity Large Hadron Collider (HL-LHC) project [2] is a series of upgrades to LHC infrastructure that will allow the LHC to collect approximately ten times more data than in the initial design by \sim 2030. The increase in LHC beam intensity will result in a large increase in collision rate that will make accessible and improve statistics on several measurements of interest [3], many only possible at the LHC and the energy frontier. The increase in beam intensity will also increase the level of background radiation, requiring major upgrades to the experiments used to record the outcomes of the particle collisions.

The ATLAS experiment [4] is one of the LHC's general-purpose particle detector arrays, positioned around one of the collision points of the LHC. During the 2019-2022 Long Shutdown of the LHC, the most complex upgrade of the ATLAS experiment is the replacement of the small wheels of the muon spectrometer with the so-called New Small Wheels (NSWs) [5].

The detector upgrade addresses both the expected decrease in hit efficiency of the precision tracking detectors and the high fake trigger rate expected in the muon spectrometer at the HL-LHC. The NSWs are made of two different detector technologies: micromegas and small-strip thin gap chambers (sTGCs). Micromegas are optimized for precision tracking while sTGCs are optimized for rapid triggering, although each will provide complete coverage and measurement redundancy over the area of the NSWs. Eight layers each of sTGCs cover the NSWs. Practically, countries involved in detector construction created quadruplet modules of four sTGCs glued together that were arranged and installed over the area of the NSWs once they arrived at CERN. Teams across three Canadian institutions built and characterized 1/4 of all the required sTGCs.

The sTGCs are gas ionization chambers that consist of a thin volume of gas held between two cathode boards. One board is segmented into strip readout electrodes of 3.2 mm pitch. The position of the particle track in the most physically interesting coordinate can be reconstructed from the strip signals [5]. The sTGCs achieved the design track spatial resolution in the precision coordinate of less than 100 μm per detector plane that will allow them to achieve a 1 mrad track angular resolution using the 8 layers of sTGC on the NSW [6, 5]. The NSW measurement of the muon track angle will be provided to the ATLAS trigger and used to reject tracks that do not originate from the interaction point [5].

The precise measurement of a muon track angle depends on knowing the position of each readout strip within the ATLAS coordinate system. To achieve this, the position of specific locations on the surface of sTGC quadruplets will be monitored by the ATLAS alignment system to account for time-dependent deformations [5]. Within a quadruplet module, the strip positions could have been shifted off of nominal by non-conformities of the strip pattern etched onto each cathode boards [7] and shifts between strip layers while gluing sTGCs into quadruplets.

An x-ray gun was used to measure the offset of strips from their nominal position at the locations that will be monitored by the ATLAS alignment system thereby providing, locally, an absolute “as-built” strip position within the ATLAS coordinate system. Estimates of the “as-built” positions of every readout strip are obtained by building an alignment model from the available x-ray measurements [8].

The technique of measuring the “as-built” strip positions using x-ray data has never been used before and must be validated. This thesis describes the use of cosmic ray data, recorded to characterize the performance of each Canadian-made sTGC module, to validate the x-ray strip position measurements. A description of how this work fits within the overall alignment scheme of the NSWs is also presented.

Chapter 2 gives a brief overview of high energy particle physics necessary to understand the physics motivation of the HL-LHC and NSW upgrades. Chapters 3 and 4 present additional

details on the LHC, ATLAS, the NSWs, and sTGCs. In Chapter 5, the cosmic ray testing procedure and how the position of the strips can be probed with cosmics data is presented. Chapter 6 introduces the x-ray method, and in Chapter 7, the x-ray offsets are validated with cosmic muon data. The thesis concludes with a summary and outlook in Chapter 8.

Chapter 2

High energy particle physics

Particle physics aims to study the elementary constituents of matter. Understanding the fundamental building blocks and how they interact provides insight into how the early universe evolved to the forms of matter we observe today. This chapter introduces general concepts in particle physics relevant to understanding the physics goals of the High-Luminosity LHC (HL-LHC) and NSWs upgrade.

The information on particle physics and the SM presented here is rather general; the interested reader is referred to [9, 10, 11] for more information.

2.1 The Standard Model

The Standard Model (SM) is a theoretical framework developed in the early 1970's that describes the observed elementary particles and their interactions. It is built on a collection of quantum field theories and has been remarkably successful at predicting experimental observations, including but not limited to the existence of the top quark [12], the tau neutrino [13] and the Higgs boson [14, 15].

The known elementary particles described by the SM are represented in Figure 2.1. There are 12 matter particles (six quarks and six leptons), 4 force-mediating particles, and the Higgs boson. Each matter particle has a corresponding anti-matter particle with the same mass but opposite charge, not represented in Figure 2.1. The different forces of nature are understood to be the result of the exchange of force-mediating particles between interacting (coupled) particles. Photons are mediators of the electromagnetic force, W⁺/- and Z bosons are mediators of the weak force, and gluons are mediators of the strong force. At high

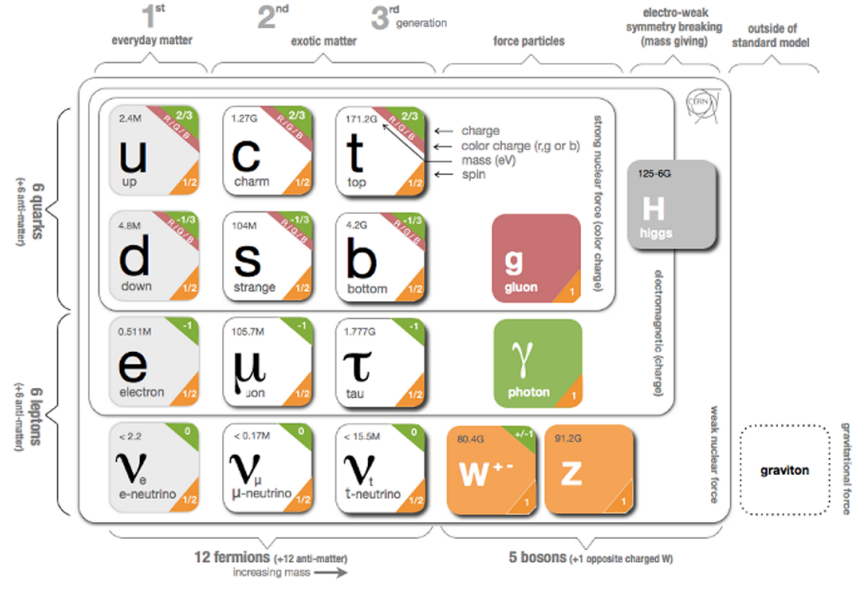


Figure 2.1: Schematic diagram of all elementary particles in the SM. Particles are grouped according to their properties and the forces through which they interact with other particles [16].

energy, the SM describes the electromagnetic and weak forces as stemming from a unified electroweak force. The Higgs boson field interacts with the particles mediating the unified electroweak force to distinguish the weak and electromagnetic forces from each other at lower energies and give particles (except neutrinos) a mass. This is called electroweak symmetry breaking.

Quarks are matter particles that are sensitive to all forces; notably they are the only matter particles sensitive to the strong force. Protons and neutrons are made up of quarks and gluons, and the strong force is responsible for their existence and mutual attraction into nuclei [17]. Leptons are particles not sensitive to the strong force. Charged leptons include the electron, which once part of atoms is responsible for chemistry. Of particular importance for this thesis is the charged lepton called a muon. It is like the electron but its mass is ~ 200 times larger than that of the electron. Muons have a lifetime of $2.2 \mu\text{s}$ [11] and decay predominantly as $\mu \rightarrow e^- \bar{\nu}_e \nu_\mu$. Neutrinos are neutral, almost massless leptons that only interact through the weak force.

Common matter is made up of the lightest constituents of the SM: up and down quarks, electrons and photons. The other particles are produced in high-energy environments but then decay to the lightest constituents. Such high energy environments include the conditions present in the early universe [18], astrophysical sources, and particle accelerators. The presence of the particles of the SM at the beginning of the universe means that their interactions and decays are fundamental for the study of the evolution of the early universe [18]. Many high energy astrophysical sources, like supernovae, generate particles that rain down on Earth as cosmic rays [19]. Particle accelerators have been built to create controlled environments of high-rate, high-energy particle collisions at high energy where the production and decay of elementary particles can be directly studied.

2.2 Beyond the Standard Model

Despite its success at describing most experimental observations to date, there is ample evidence that the SM is not a complete description of natural phenomena at the smallest scales. For example, the SM has a large number of free parameters, the values of which have to be fine-tuned to fit experimental observations. This is part of the so-called “naturalness” problem.

Furthermore, the SM provides no explanation for several open questions in particle physics. First, neutrinos in the SM are assumed to be massless and do not gain mass in the same way as the other particles. However, neutrinos were confirmed to change between their different flavours (ν_e , ν_μ , ν_τ) in 2013 [20], which can only occur if neutrinos do have mass [21]. The neutrino mass requires physics beyond the Standard Model [22]. Second, several astrophysical and cosmological measurements suggest the presence of “dark matter” making up 85 % of the matter content of the universe [23]. The nature of dark matter is unknown and so far there is no SM explanation [24]. Third, the SM does not explain the origin and nature of the matter-antimatter asymmetry that produced our matter-dominated universe. Finally, the SM does not include a description of gravity.

Theoretical extensions beyond the Standard Model (BSM) aim to address some of these questions, often predicting existence of yet-unseen elementary particles or physics phenomena beyond those predicted by the SM. These hypothetical new physics phenomena or new particles can be searched for at particle accelerators.

2.3 Studying high energy particle physics with accelerators

In particular, particle accelerators of increasingly higher energy have a long history of enabling the discovery of predicted particles. These include, for example, the discovery of the W [25, 26] and Z bosons [27, 28], the top quark [29, 30], and most recently, the Higgs boson [31, 32]. The discovery of the Higgs boson marked the completion of the SM as it is known today.

Based on the established success of the SM, there are two approaches to particle physics research. One approach is to search for the existence of new physics phenomena predicted to exist in BSM theories and the other is to test the validity of the SM to a high degree of accuracy to search for flaws in the model. Standard Model predictions are generally expressed in terms of the probability of a specific physics process to occur, expressed as a cross section in units of barns (with 1 barn = 10^{-28} m²). As an example, Figure 2.1 shows a summary of cross section measured for different physics processes using the ATLAS experiment and their comparison with the predictions of the SM. Most cross section measurements agree well within one standard deviation with the SM predictions.

Particle accelerators provide a controlled and high-collision rate environment that makes them ideal places to search for new physics phenomena and to carry out systematic tests of the SM. The LHC is the highest energy collider in the world so it can access physics that no other accelerator can. A description of the LHC and the ATLAS detector are provided in the next chapter.

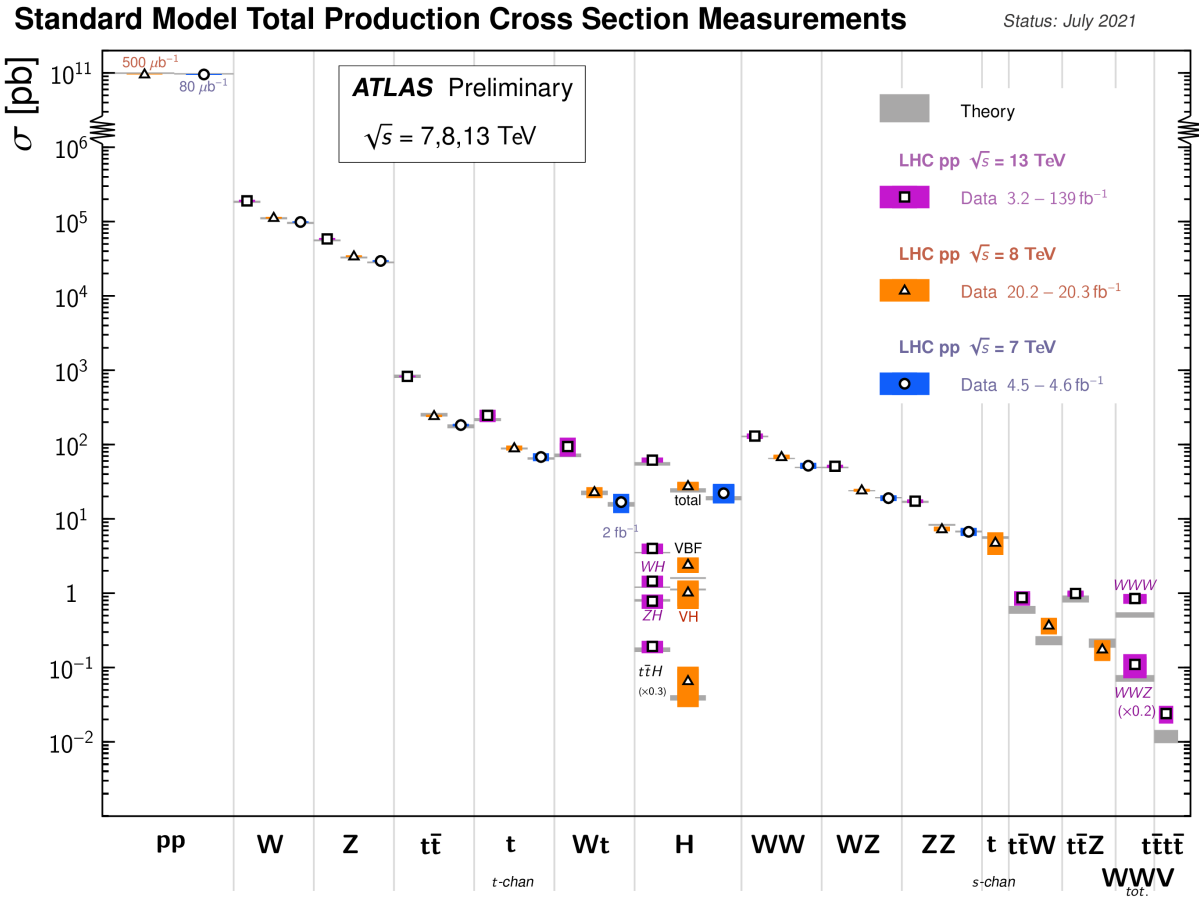


Figure 2.2: Production cross sections of different final states measured by the ATLAS experiment at the LHC. Comparison with the SM theory predictions is also shown [33].

Chapter 3

The LHC and the ATLAS experiment

The Large Hadron Collider (LHC) is the world’s most energetic particle accelerator and the ATLAS experiment is used to record the results of particle collisions at the LHC. In this chapter, details about both that are necessary to understand the High-Luminosity LHC (HL-LHC) upgrade project and the ATLAS experiment’s New Small Wheels (NSWs) upgrade are presented.

3.1 The Large Hadron Collider

The LHC is an accelerator 27 km in circumference and located \sim 100 m underground at the CERN laboratory near Geneva, Switzerland [1]. It has two beam pipes within which bunches of protons counter-circulate before being collided in the center of one of four major experiments, such as the ATLAS experiment (discussed in Section 3.3). Protons are guided on the circular trajectory using 1232 superconducting dipole magnets capable of a maximum field of 8.33 T. Radio-frequency accelerating cavities are used to accelerate protons to a the maximum design energy of 7 TeV [34]. During LHC Run-1 (2011-2012), protons were collided at a collision center-of-mass energy of 7 TeV and 8 TeV [35]. During LHC Run-2 (2015-2018), the center-of-mass energy of proton collisions was increased to 13 TeV [36], close to the maximum design value of 14 TeV [34]. It is not actually the protons that interact, but the constituent quarks and gluons that each carry some fraction of the energy and momentum of the collisions.

Luminosity

The number of proton-proton interactions generated by the LHC directly affects the statistics

available to make measurements of interaction cross sections. Predicting the number of proton-proton interactions requires defining a metric called luminosity [11]. The luminosity of a particle collider is the number of particles an accelerator can send through a given area per unit time. It is calculated from the measurable quantities in Equation 3.1:

$$\mathcal{L} = \frac{f N_1 N_2}{4\pi\sigma_x\sigma_y}, \quad (3.1)$$

where f is the frequency of the bunch crossings (40 MHz, corresponding to 25 ns), N_1 and N_2 are the number of protons in each bunch ($\sim 10^{11}$ protons / bunch), and σ_x and σ_y are the RMS of the spatial distributions of the bunch. Therefore, luminosity is a property of accelerator beams, which are set by the capabilities of the accelerator. The design luminosity of the LHC was $10^{34} \text{ cm}^{-2}\text{s}^{-1}$. The units of luminosity are an inverse area per unit time; multiplying the luminosity by the cross section of a given process gives the expected rate for that process.

Integrating the *instantaneous* luminosity (Equation 3.1) over a period of data collection time gives the integrated luminosity,

$$L = \int \mathcal{L}(t) dt \quad (3.2)$$

which is related to the total number of interactions. In this way, the luminosity is the link between the accelerator and the statistical power of measurements to be made with the data collected. So far, the LHC provided an integrated luminosity of 28.26 fb^{-1} in Run-1 [35] and 156 fb^{-1} in Run-2 [36].

3.2 The High-Luminosity LHC

At the end of the LHC program in 2025, the statistical gain on measurements in running the LHC further will become marginal. The HL-LHC [2] project consists of the upgrade of LHC infrastructure to achieve a nearly ten fold increase in instantaneous luminosity, thereby improving measurement statistics as well. Also, some systems will need repair and replacement to operate past ~ 2020 . The LHC will continue to be the most energetic accelerator in the world for years to come and is the only accelerator with enough energy to directly produce the Higgs boson and top quarks. Therefore, the European Strategy for Particle Physics made it a priority “to fully exploit the physics potential of the LHC” with “a major luminosity upgrade” [37]. The goal is for the HL-LHC to provide an integrated



Figure 3.1: The LHC/HL-LHC timeline [38]. The integrated luminosities collected and projected for each run of the LHC are shown in blue boxes below the timeline and the center of mass energy of the collisions is shown in red above the timeline. The top blue arrow labels the run number. The acronym “LS” stands for “long shutdown” and indicates periods where the accelerator is not operating. During the shutdowns, upgrades to the LHC and the experiments are taking place. This timeline was last updated in January, 2021, and reflects changes in the schedule due to the ongoing pandemic.

luminosity of 3000 fb^{-1} in the 12 years following the upgrade. The luminosity actually achieved will depend on a combination of technological advances and upgrades in progress that affect the factors contributing to luminosity defined in Equation 3.1 [2]. Figure 3.1 shows the projected schedule of the HL-LHC upgrades and operation [38].

One of the most anticipated measurements at the HL-LHC is the value of the triple-Higgs coupling. Measuring the coupling will allow the determination of the shape of the Higgs potential responsible for electroweak symmetry breaking. Any discrepancy with respect to the SM prediction will show that there must be other sources of electroweak symmetry breaking, and hence physics phenomena beyond the SM. The LHC is the only accelerator where the Higgs boson can be produced directly so it is the only place where the triple-Higgs coupling could be measured. The HL-LHC upgrade is required to produce a significant

sample of Higgs produced in pairs to make a statistically meaningful measurement [3, 39]. Accordingly, detector sensitivity to various Higgs decays will be important at the HL-LHC.

3.3 The ATLAS experiment

The ATLAS experiment [4] was designed to support all the physics goals of the LHC. It is 44 m long and 25 m in diameter, and weighs 7000 tonnes. The ATLAS experiment is centered around one of the LHC’s interaction points (a place where the beams collide). As shown schematically in Figure 3.2, ATLAS consists of an array of particle detector subsystems arranged concentrically around the beam pipe. The ATLAS experiment has cylindrical symmetry to accommodate the beam pipe and other construction constraints while providing 4π coverage around the interaction point. In reference to the cylindrical geometry of the experiment, it is helpful to separate the subsystems of ATLAS into the so-called “barrel” and “endcap”/“forward” regions.

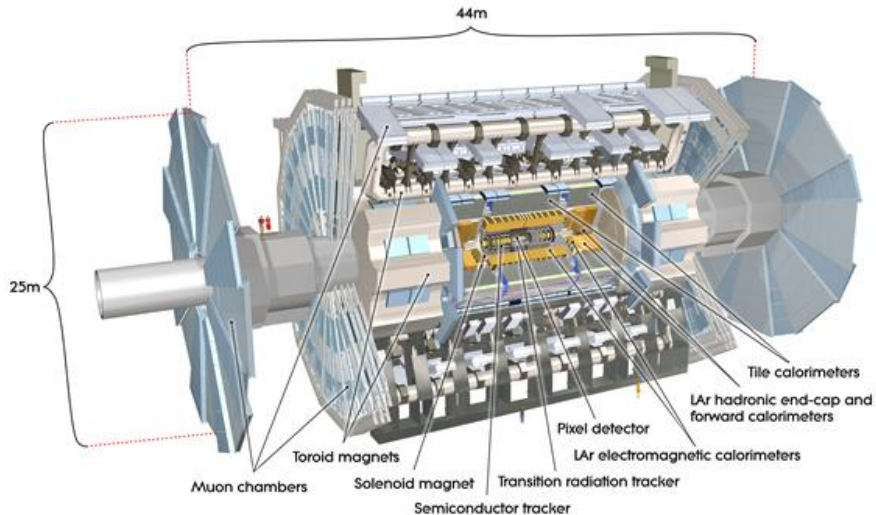


Figure 3.2: Schematic diagram of the ATLAS experiment, with the various detector subsystems labelled [4].

For analysis purposes, a spherical coordinate system is defined. The azimuthal angle ϕ is measured around the beampipe and the polar angle θ is measured from the beam pipe. The polar angle is more often expressed in terms of pseudo-rapidity, defined as $\eta = -\ln \tan(\theta/2)$. Pseudo-rapidity values vary from 0 (perpendicular to the beam) to $\pm\infty$ (parallel to the

beam, defined as the z-direction) and is an approximation to the rapidity of a particle when its momentum is much greater than its mass. It is useful to describe the direction of outgoing particles in proton-proton collisions because differences in rapidity are invariant to a Lorentz boost along the beam direction.

The ATLAS experiment provides identification and kinematic measurements for each particle created after the initial collision, which is done by assembling offline the information recorded by each subsystem. With this information, signatures of processes of interest can be identified and studied. An overview of the main ATLAS subsystems is given below, starting with the innermost subsystem and moving outwards from the beam pipe.

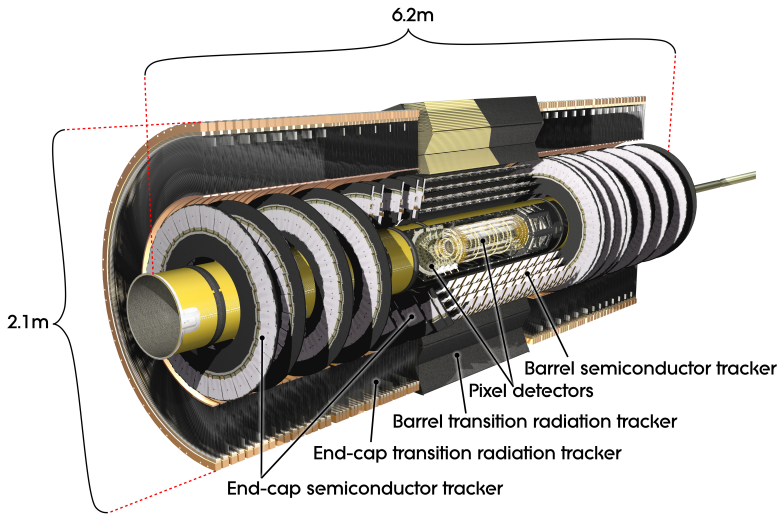


Figure 3.3: Schematic diagram of the ATLAS experiment’s inner detector, with the different segments and the technology used labeled [4].

The inner detector

The inner detector [40, 41] (Figure 3.3) is for precise measurements of charged particle trajectories, measurement of primary and secondary interaction vertices and assistance in the identification of electrons. A 2 T solenoid with field parallel to the beam bends the trajectory of outgoing charged particles. A measurement of the bending radius of each charged particle provides information about its momentum. The innermost part of the inner tracker is made of high-resolution semiconductor pixel and strip detectors while the outermost part is made of straw-tubes. The straw tubes are used in the trajectory measurements but they are also interspersed with material designed to enhance the creation of transition radiation.

Transition radiation occurs when a highly relativistic charged particle traverses a material boundary [42]. The amount of transition radiation emitted by a charged particle is detected by the straw-tubes and is used to identify electrons.

Calorimetry system

Electromagnetic and hadronic sampling calorimeter units are used to record the energy of electrons, photons and jets¹. A combination of liquid-argon (LAr) electromagnetic and hadronic calorimeters [43] and tile-scintillator hadronic calorimeters [44] cover the rapidity range $|\eta| < 4.9$, as shown in Figure 3.4.

Sampling calorimeters have alternating layers of dense material and material that can measure the amount of ionization by charged particles. The dense material causes incoming charged particles to shower into lower energy particles and deposit their energy in the sensitive volume. Only muons and neutrinos are known to pass the calorimeters to the muon spectrometer without being absorbed.

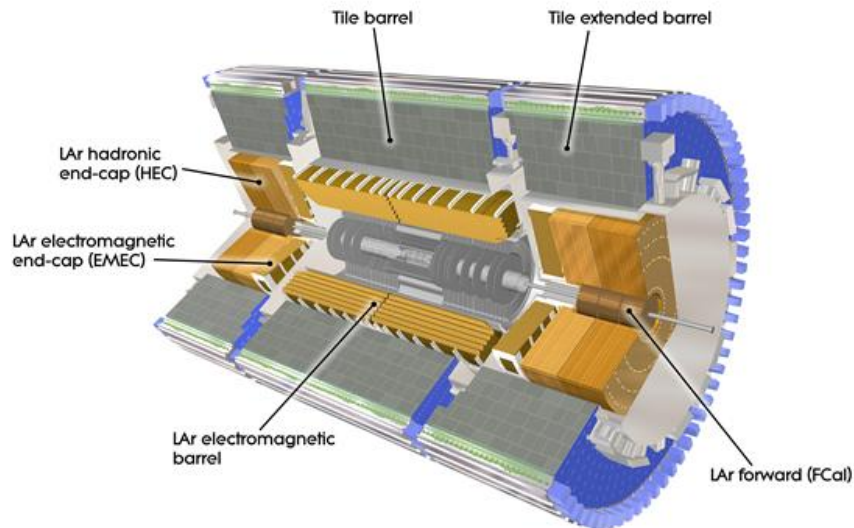


Figure 3.4: Schematic diagram of the ATLAS calorimeter system, with the different segments and the technology used labeled [4].

¹When quarks or gluons are expelled in a high energy collision, they create collimated groups of hadrons called jets because they carry a charge called “colour”, and nature only allows “colourless” combinations to exist [42].

Before moving onto the next detector layer of the ATLAS experiment, the muon spectrometer, the trigger system is introduced because details about how the muon spectrometer feeds the trigger system partially motivate the NSW upgrade.

Trigger system

It would be impossible to record all the data from bunch crossings every 25 ns, corresponding to a rate of ~ 40 MHz. The ATLAS experiment has a multi-level trigger system to select events of interest for permanent storage. The Level-1 (L1) hardware trigger [45] uses partial-granularity information from the muon spectrometer and calorimeters to trigger on high p_T muons, electrons, jets, missing transverse energy, and τ decaying to hadrons. After Run-3 an upgrade of the trigger system will allow a maximum trigger rate of 1 MHz with a latency of 10 μ s [46], but for now the working limits are a rate of 100 kHz [47] and 2.5 μ s [45].

The L1 trigger is used to define regions of interest that are fed into the software high level trigger (HLT) [48], in which the full granularity of the muon spectrometer and calorimeter are used with information from the inner detector to reduce the trigger rate to 1 kHz. Events that satisfy at least one of the L1 and HLT trigger criteria are recorded to permanent storage for offline analysis.

Muon spectrometer

The muon spectrometer [49] consists of multiple layers of tracking chambers embedded in a 2 T magnetic field generated by an air-core superconducting toroid magnet system. Figure 3.5a shows a schematic diagram of the layout of the different chambers and of the toroid magnets [4]. The trajectory of a muon is reconstructed from the information recorded by the different types and layers of tracking chambers. The amount of bending in the magnetic field provides a measure of the muon's momentum. In the barrel section of ATLAS, the toroidal magnetic field is created by eight coils bent into the shape of a "race-track" and symmetrically arranged around the beampipe. In the forward region, two end-cap toroids, each with eight smaller racetrack-shaped coils arranged symmetrically around the beam pipe are inserted in the ends of the barrel toroid [50].

The muon spectrometer is separated into detectors used for precision offline tracking and for triggering purposes. Three layers of monitored drift tubes (MDTs) or cathode strip chambers (CSCs) are used for tracking. The position of the muon track in each of the three layers allows reconstruction of the bent trajectory of a muon and hence its momentum. To satisfy the muon spectrometer target momentum resolution of $\Delta p_T/p_T < 1 \times 10^{-4}$ p / GeV for $p_T < 300$ GeV and a few percent for lower p_T muons, the MDTs and CSCs were designed to achieve a spatial resolution of 50 μ m each. Accordingly, an optical alignment system was designed to monitor and correct for chamber positions [49, 52].

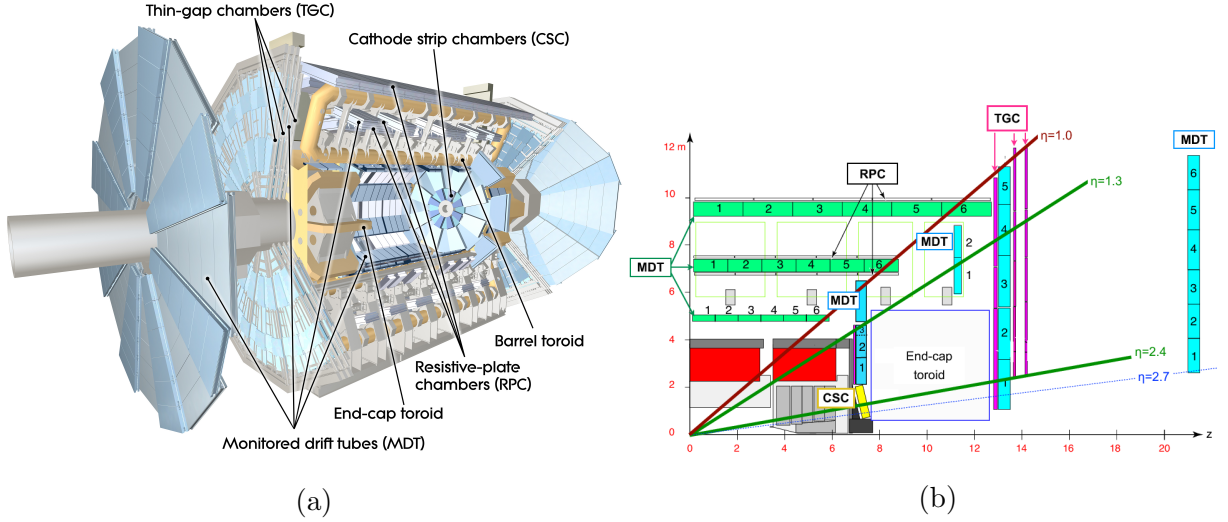


Figure 3.5: Schematic diagram of the ATLAS muon spectrometer. Figure (a) shows a 3D projection of the system with the different types of chambers and different parts of the toroidal magnet system labeled [4]. Figure (b) shows a projection of one quarter of the muon spectrometer, with the interaction point in the bottom left corner. The small wheel is just left of the end cap toroid, the big wheel is to its right, and the outer wheel is the rightmost structure [51].

Resistive plate chambers (RPCs) are used for triggering in the barrel and thin-gap chambers (TGCs) are used for triggering in the endcaps. The positions of each type of chamber are sketched in Figure 3.5b. The endcap section of the muon spectrometer consists of three sections, the small wheel, big wheel, and outer wheel – ordered by proximity to the interaction point. In Run-1, low (high) p_T muons were triggered on if two (three) of the RPC or TGC layers around the big wheel fired in coincidence, for the barrel and endcaps respectively [45]. After Run-1 it was discovered that up to 90% of the triggers in the endcap were fake, caused by background particles generated in the material between the small wheel and the big wheel [5]. To reduce the fake rate in Run-2, the TGCs on the inside of the small wheel also had to register a hit. The added condition reduced the trigger rate by 50% in the range $1.3 < |\eta| < 1.9$ [47]. The effectiveness of the solution was limited since the $|\eta|$ -range of the small wheel TGCs was limited to $1.0 < |\eta| < 1.9$ and the spatial resolution of the small wheel TGCs is coarse [5].

With the foreseen increase in luminosity at HL-LHC, it is a priority to upgrade the ATLAS detector to further reduce the muon trigger fake rate in the forward region. The New Small Wheels being commissioned to replace the original ATLAS muon small wheels will address this challenge.

Chapter 4

The New Small Wheels

4.1 Motivation for the New Small Wheels

The hit rate of all detector systems will significantly increase during HL-LHC operation because of the increase in luminosity. The increased rate presents a challenge for both the tracking and triggering capabilities of the muon spectrometer [5].

In terms of precision tracking, the maximum hit rate in the MDTs is expected to reach above 300 kHz by the end LHC operation. At this rate, the hit efficiency of MDTs decreases by 35%, mostly due to the long dead-time of the chambers. Losing hits in the small wheel will reduce the high p_T muon momentum resolution. The decrease in resolution will affect the ability to search for, for example, the decay of hypothetical heavy bosons (W' , Z') or other hypothetical particles beyond the SM [3].

Already during LHC Run-2 operation, the forward muon trigger system had to cope with a very high fake rate, even with the inclusion of TGC data from the small wheel as part of the trigger criteria. At the luminosity expected in Run-3, it is estimated that 60 kHz out of the maximum L1 trigger bandwidth of 100 kHz would be taken up by forward muon triggers. To address this challenge, a possible solution would be to raise the minimum p_T threshold from 20 GeV to 40 GeV. However, this would have an adverse impact on the ability to study several physics processes of interest that depend on low p_T muons, particularly the Higgs decay to two muons, the Higgs decay to two tau leptons and hypothetical particle decays beyond the SM [5].

The NSWs will address both of these problems. They will be made of precision tracking chambers suitable for the expected hit rates during the HL-LHC and triggering chambers capable of 1 mrad track angular resolution. The idea behind the design triggering capability

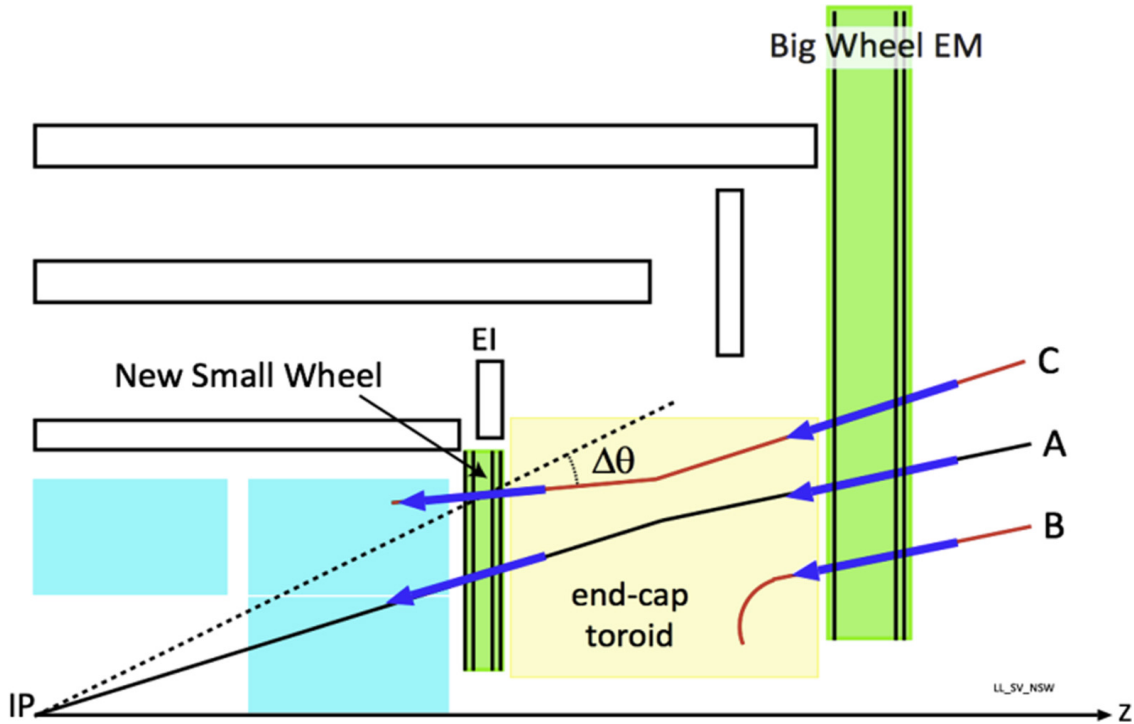
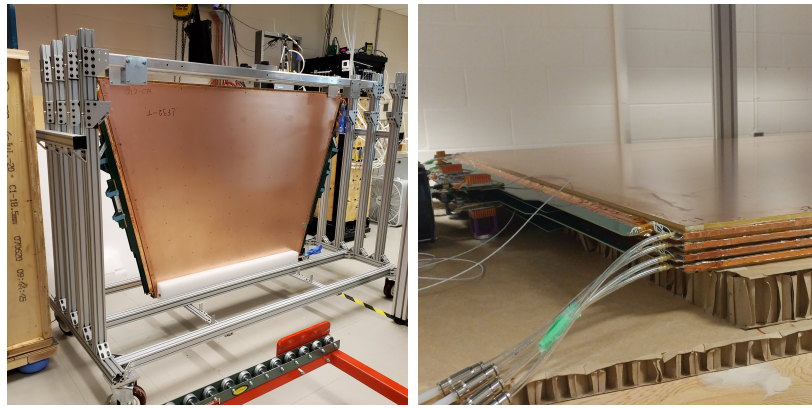


Figure 4.1: A schematic diagram of a quarter cross section of the ATLAS muon spectrometer, with the interaction point (IP) in the bottom left corner. Three possible tracks are labeled. Ideally, track A would be triggered on while track B and C discarded. With the old small wheel, all three tracks would be recorded. With the NSW, only track A would be recorded [5].

of the chambers is to allow matching of track segments measured by the NSW with track segments from the big wheel to discard tracks not originating from the interaction point. Figure 4.1 illustrates this point: the Run-2 trigger system would have triggered on all three tracks (A, B, C) while with the NSW the trigger system would only trigger on track A. The NSWs will therefore make it possible to maintain a low muon p_T trigger threshold and maintain an adequate muon momentum resolution during HL-LHC operations, which will allow the full exploitation of the physics potential of this research program [5].



(a) A sTGC quadruplet module. The left image highlights the trapezoidal shape of a quadruplet module. The right image shows the corner at the short edge, where the four sTGC layers and each layer's gas inlet are visible. The gas outlets and high voltage cables are located along the long edge near the corner in the back left of the photo. The green printed circuit boards along the sides are the adaptor boards where the front end electronics are attached.



(b) Left: A sTGC wedge. The white frame outlines the individual quadruplet modules that have been glued together into a wedge. Right: A completed sector, with two sTGC wedges on the outside and two micromegas wedges on the inside.



(c) A picture of one of the two NSWs. All sectors except one large sector at the top are installed, revealing two of the smaller sectors that are normally hidden under the large sectors and support bars. The NSWs are 9.3 m in diameter.

Figure 4.2: Images showing different stages of NSW construction.

4.2 Design of the NSWs

The NSWs are made with two detector technologies: micromegas and small-strip thin gap chambers. Eight layers of each cover the entire area of the wheel. Micromegas are designed to be the primary precision tracking detectors and sTGCs the primary triggering detectors, but both technologies offer full redundancy by being capable of providing both precision measurements and trigger information. Both types of detectors were designed to achieve spatial resolution better than $\sim 100\text{ }\mu\text{m}$ per layer. Four chambers are glued together to create quadruplet modules of each detector type. Quadruplets of different sizes, most shaped as trapezoids, are assembled into wedges. Two sTGC wedges and two micromegas wedges are layered to create sectors (with the sTGC wedges on the outside) [5]. Different stages of the construction process are shown in Figure 4.2. At the time of writing, the assembly of the NSWs has just been completed. The first NSW has been lowered into the ATLAS cavern and is being commissioned and the second will be lowered shortly.

4.3 Small-strip thin gap chambers

The sTGCs are gas ionization chambers operated with a gas mixture of CO₂:n-pentane with a ratio of 55%:45% by volume. Gold-plated tungsten anode wires, 50 μm in diameter and with 1.8 mm pitch, are suspended between two cathode planes made of FR-4 printed circuit board, each 1.4 mm away (see Figure 4.3). One cathode board is segmented into copper pads of varying area (with a typical size of $\sim 300\text{ cm}^2$ each), and the other is segmented into copper strips of 3.2 mm pitch running lengthwise perpendicular to the wires. High voltage is applied to the anode wires and the cathode planes are grounded [5, 53]. When a muon passes through a sTGC, it will ionize nearby atoms of the gas. The electrons drift towards the anode wires and in the high electric field region near the wires generate an ionization avalanche [54]. The motion of the ions and free electrons generates small currents on the nearby wire and capacitatively-coupled strip and pad electrodes [5]. The gas mixture was chosen to absorb excess photons produced in the avalanche that delocalize the avalanche signal [55] and saturate many strip electrodes, preventing the formation of streamers [42]. This allows the chambers to be run at a higher high-voltage providing a faster response and higher signal [55]. A carbon coating and pre-impregnated sheet are layered over the printed circuit board of the cathode board, as shown in Figure 4.3. The resistivity of the carbon coating and capacitance of the pre-impregnated sheet tune the spread of the charge distribution [56] and the speed of the response [57] to optimize the rate capability. The combined information from the strip readout electrodes and wires provide the location where the muon passed through the chamber. The small pitch of the strip readout electrodes is

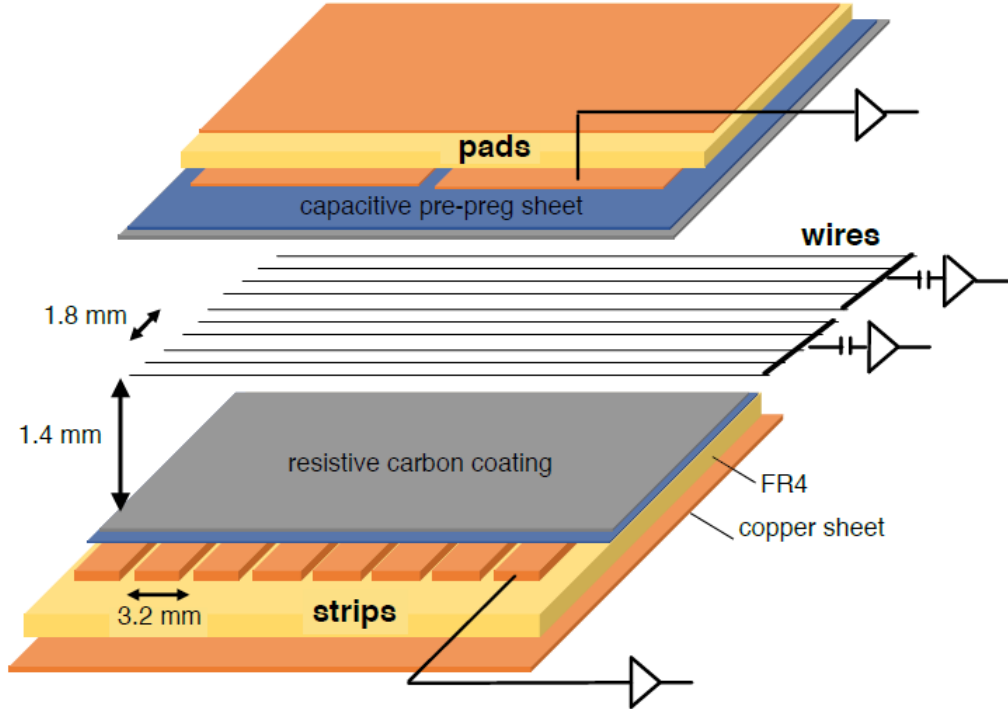


Figure 4.3: Internal structure of an sTGC, zoomed into the area under a pad. High voltage is applied to wires suspended in the gas volume to create an electric field. A passing muon causes an ionization avalanche that is picked up by the wire, strip and pad electrodes [8].

what allows the quadruplets to deliver good track angular resolution to improve the fake trigger rate and meet the precision tracking requirements [5].

A 3-out-of-4 coincidence in pad electrodes from each layer of a quadruplet defines a region of interest where the strip and wire electrodes should be read out. The pad triggering scheme greatly reduces the number of electrodes that require readout so that a track segment of the required angular resolution can be provided quickly enough to the hardware trigger [5].

Signal is read out from groups of 20 successive wires, so the position resolution in the direction perpendicular to the wires is 10 mm per plane. The wires give the azimuthal coordinate in ATLAS so the position resolution in this direction is sufficient. Good resolution on the η coordinate, perpendicular to the strips, is important [5]. In a test beam environment, the strip spatial resolution of a single sTGC was measured to be 45 microns for muons

perpendicularly incident on the surface of the sTGC. Although the spatial resolution worsens as function of muon angle measured from normal incidence [58], when four sTGCs are glued together into a quadruplet the design angular resolution of 1 mrad in the strip coordinate is achievable [5, 53].

To achieve the required track angular resolution once installed in ATLAS, the absolute position of each sTGC strip within the ATLAS coordinate system must be accurately known. The degree of accuracy required is on the order of the position resolution of the chambers, $\sim 100 \mu\text{m}$. The NSW alignment system, detailed in Section 4.5, will monitor the position of alignment platforms installed on the surface of the wedges. The alignment platforms are installed with respect to an external reference on the sTGCs: two brass inserts on each strip layer on one of the angled sides of each quadruplet (shown in Figure 4.4). So the challenge of monitoring the position of the strips in ATLAS was separated into two steps: first, infer the position of the strips with respect to the brass inserts using the sTGC design geometry; second, use the alignment system to monitor the position of the alignment platforms. The next section provides some pertinent details on the sTGC construction process, with steps that affect the position of the strips with respect to the brass inserts highlighted.

4.4 sTGC Quadruplet Construction

Five countries were responsible for producing sTGC quadruplets of varying geometries for the NSW: Canada, Chile, China, Israel and Russia. Canada was responsible for the construction of one quarter of the required sTGCs, of three different quadruplet geometries. The steps of the construction process in each country were similar [5]. The process followed in Canada is detailed here.

A research group at TRIUMF in Vancouver, British Columbia was responsible for preparing the cathode boards. The boards were made and the electrodes etched on at a commercial laboratory, Triangle Labs, in Carson City, Nevada. Once completed they were sent to TRIUMF to be sprayed with graphite and to have support structures glued on [7]. The boards are commercial multilayer printed circuit boards, but the strip boards required precision machining to etch the strip pattern [5]. Triangle Labs also machined the two brass inserts into each strip board. A coordinate measuring machine (CMM) was used to accurately measure the position of a set of reference strips on each board. Four quality parameters describing non-conformities in the strip pattern of each board with respect to the brass inserts were derived from the data and the results are available on a QA/QC database. The parameters – offset, angle, scale and nonparallelism – and the CMM data collection is described in full in [7]. Due to time constraints, tolerances on the non-conformities in the etched strip pattern



(a) Brass insert near long edge.

(b) Brass insert near short edge.

Figure 4.4: The brass inserts sticking out from the gas volumes of an sTGC quadruplet. These inserts were pressed against alignment pins when the individual sTGCs were being glued together.

with respect to the brass inserts were loosened, with the condition that the strip positions in ATLAS would have to be corrected for [7].

The prepared boards were sent to Carleton University in Ottawa, Ontario for construction into sTGCs and quadruplets. First, the wires were wound around the pad cathode boards using a rotating table and the wires were soldered into place. A wound pad cathode board was held by vacuum on a granite table, flat to within 20 μm , and a strip cathode board glued on top to create an sTGC. Holding one sTGC flat with the vacuum, another was glued on top to create a doublet, then two doublets were glued together to create a quadruplet. When gluing sTGCs together, the brass inserts were pushed against alignment pins with the goal of keeping the strip layers aligned within tolerance. However, non-conformities in the shape of the brass inserts, non-conformities in the position of the alignment pins and shifts between sTGCs while the glue cured resulted in misalignments between the brass inserts and strip layers. Precise alignment of the pad boards or wires with respect to the strip boards did not have to be so tightly controlled because pads and wires do not measure the precision coordinate.

The Carleton team finished the quadruplets by installing adaptor boards on the angled sides of each layer that allow front end electronics to be attached. Completed quadruplets were sent to McGill University where their performance was characterized with cosmic rays. Details pertaining to cosmic ray testing of sTGC quadruplets at McGill University are described in Chapter 5. Tested quadruplets were sent to CERN where they were assembled into wedges and alignment platforms installed. The alignment platforms were installed using a jig positioned with respect to the brass inserts. Completed wedges were assembled into sectors then installed on the NSWs.

The quadruplet construction process had two steps where strip positions could be shifted off nominal. At board-level, there could be non-conformities in the etched strip pattern with respect to the brass inserts, described by the four quality parameters [7]. At the quadruplet level, misalignments between the brass inserts and strips on different layers were possibly introduced during the gluing. The result was that the brass inserts were not a reliable reference point and that the strips can be offset from their design position by up to hundreds of micrometers. Offsets in strip positions from nominal in Canadian quadruplets were shown to be random [7], so no one correction would suffice. The offsets must be measured and corrected for in the ATLAS offline software that does the precision tracking. Understanding the work ongoing to make measurements of strip position offsets and correct for them requires understanding the strategy of the NSW alignment system.

4.5 NSW alignment

The idea of the NSW alignment system is presented in [5], but the details have only been presented internally so far. After the wedges are constructed, alignment platforms are installed on every sTGC quadruplet and optical fibres routed to them, as shown in Figure 4.5. Light from the optical fibres will be monitored in real time by cameras (BCAMs) mounted on the alignment bars of the NSWs. The system will thus record the positions of the alignment platforms in the ATLAS coordinate system and any changes over time.

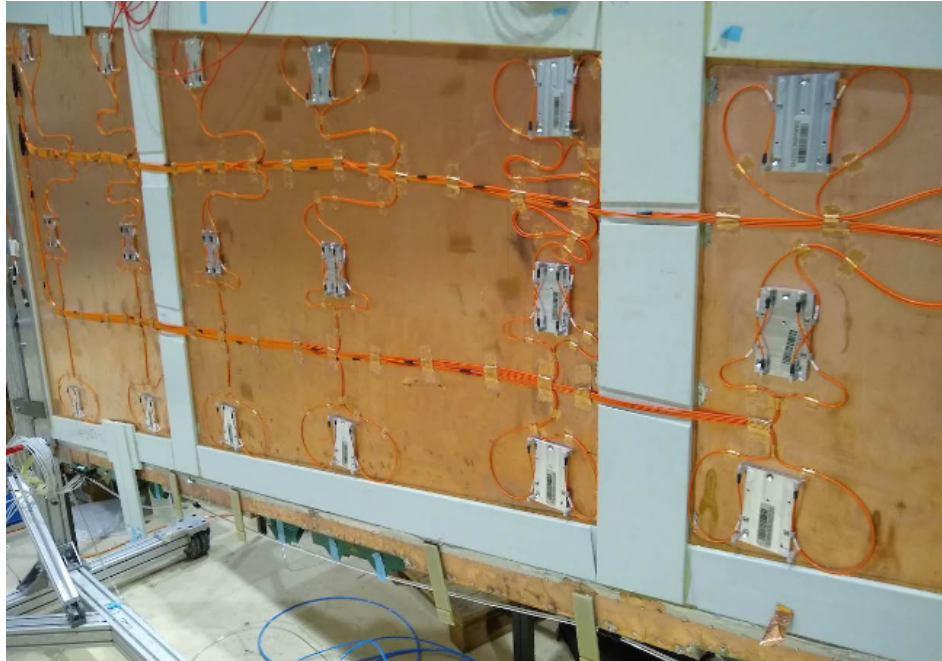


Figure 4.5: A sTGC wedge with alignment platforms (silver) installed on the quadruplet. Optical fibres (orange) are routed to the alignment platforms. Cameras on the frames of the NSWs will record light from the optical fibres to monitor in real-time the position the alignment platforms in the ATLAS coordinate system.

The original alignment scheme was to use the brass inserts as a reference between the alignment platforms and the individual strips, as shown in the solid arrows in Figure 4.6 – this will no longer work. The position of the alignment platforms will be known thanks to the alignment system, so a different method to get the position of the strips with respect to the alignment platforms is currently in its final stage of development. The technique consists of the measurement of the strip pattern offset at a few areas on the surface of a sTGC quadruplet using an xray gun mounted on the alignment platforms. The local strip pattern offset

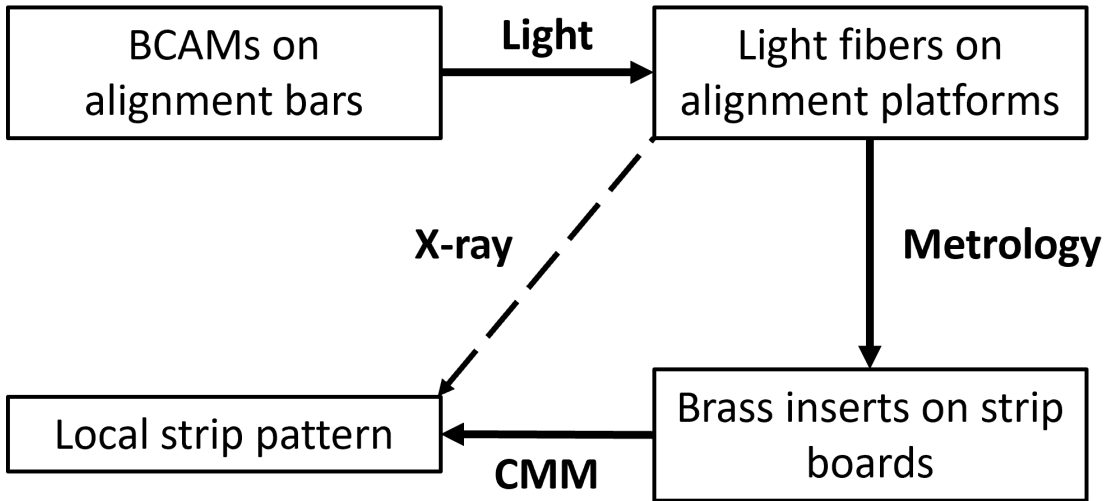


Figure 4.6: Schematic diagram showing how the different elements of the sTGC alignment system relate to one another. The solid arrows denote the planned alignment scheme. The dashed arrow shows the modification being finalized now. This figure was originally designed by Dr. Benoit Lefebvre.

with respect to nominal geometry at the location of each alignment platform is obtained by analyzing the x-ray gun beam profile. As shown in Figure 4.6, this approach essentially bypasses the need to know the position of strips with respect to the brass inserts. The alignment platforms provide the link to the nominal geometry because the nominal group of strips that should be nearest to them can be identified using the nominal geometry parameters that assume the strips are perfectly etched and aligned. Cosmic muon track positions cannot be compared to the nominal geometry because the alignment platforms are not installed when cosmics data is collected, so there is no external reference to provide a link to the nominal geometry.

The x-ray method does not have the sensitivity to measure the offset of each strip from nominal, but what can be measured instead is the offset of the strip pattern in a local area around the position of the gun. *Local offsets* are used to build an alignment model for each strip layer. Formally defined, an alignment model is a set of parameters used to estimate the “as-built” position of a strip given its nominal position. The alignment model currently being worked on takes x-ray and CMM data as input to calculate an overall offset and rotation of each strip layer with respect to nominal [8]. The alignment parameters could be described as “global”, meaning over the whole layer instead of local. Without the x-ray dataset, there would be no input to the alignment model that takes into account inter-layer misalignments

introduced during quadruplet construction.

Given that the x-ray local offsets can only be measured at positions where the gun can be attached and that they are an important part of the alignment scheme, the new x-ray measurement technique needs to be validated. The goal of this thesis is to validate the x-ray local offsets while exploring how cosmics data complements and adds to the understanding of strip positions and global alignment.

Chapter 5

Using cosmic muons to measure relative strip position offsets

At McGill University, among other quality and functionality tests, each Canadian-made quadruplet was characterized with cosmic muons. In this chapter, the experimental setup and how the data was analyzed to provide relative strip position offsets is presented. The analysis method was motivated by the how the measurements could be compared to measurements done with the x-ray method (Chapter 6) but also it stands alone as a characterization of the alignment between strips of different layers. The chapter begins with a brief introduction to cosmic rays.

5.1 Cosmic rays

The earth is being constantly bombarded by particles from the sun, galactic sources and extra galactic sources – collectively called cosmic rays [19, 11]. Cosmic rays consist mostly of protons, but also heavier ions, gamma rays and the term sometimes includes neutrinos. The primary (initial) cosmic ray interacting with the atmosphere causes electromagnetic and hadronic showers of secondary particles. Hadronic showers result from the primary cosmic ray interacting strongly with the nuclei in the atmosphere, resulting in an abundant production of pions. Charged pions predominantly decay to muons (there is a lesser contribution to the muon flux from kaons as well) [59]. The secondary muons are relativistic and thanks to time dilation their lifetime is extended as measured in the reference frame of earth, so a flux of approximately 1 muon/cm²/ min reaches the ground [11]. Measuring the muon flux and energy spectrum reveals information about primary cosmic rays [59] which is interesting

to high energy physicists and astrophysicists. The muon flux is also terribly convenient for testing muon detectors.

5.2 Experimental setup

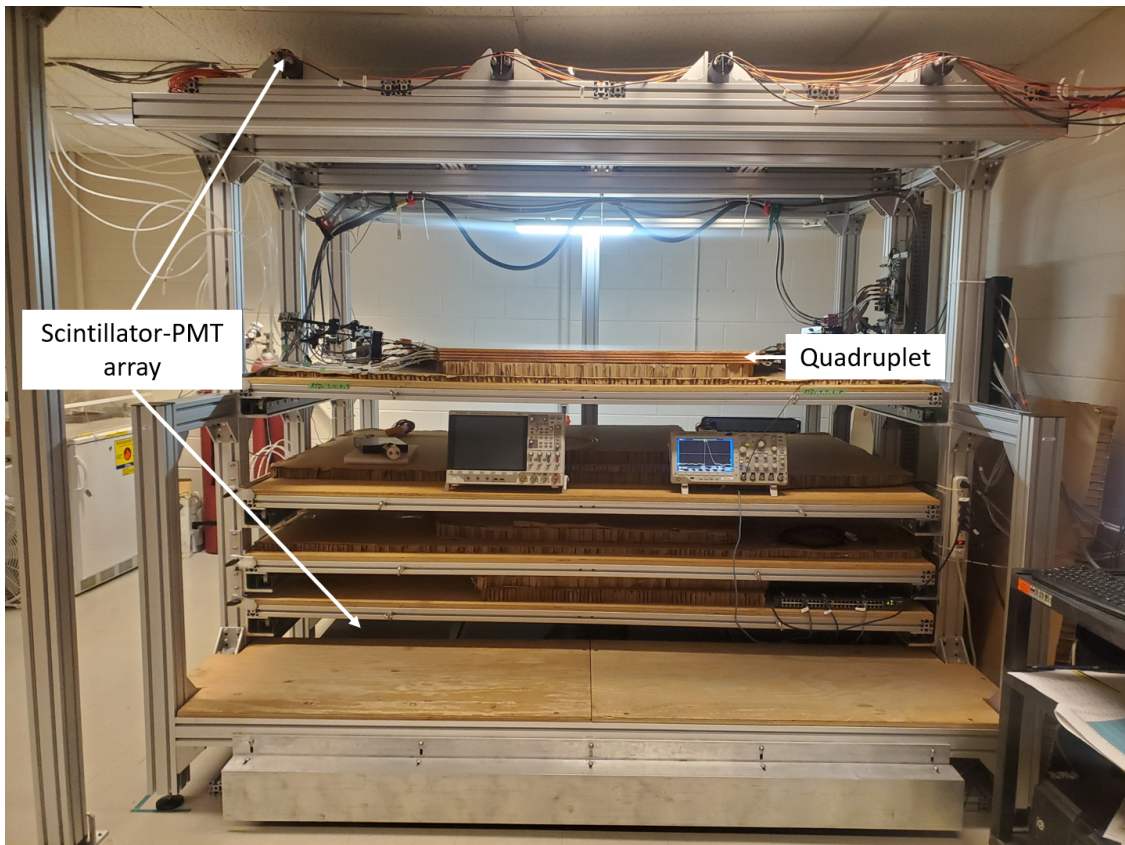


Figure 5.1: Cosmic muon hodoscope at McGill University with a sTGC quadruplet module in the test bench.

Cosmic muon characterization of sTGC quadruplet modules was done with a hodoscope, a complete description of which can be found in [58]. The quadruplet was placed in the center of the test bench. Above and below it was a layer of scintillator-PMT arrays, as shown in Figure 5.1. When a cosmic muon passed within the acceptance of the hodoscope, at least one scintillator from the top array and at least one from the bottom array fired in coincidence. A trigger signal was formed using NIM modules from the coincidence of signals from the top

and bottom arrays of scintillators. The trigger signal was passed to the front-end electronics attached to the adaptor boards of each layer of the quadruplet.

Operating the chambers also required gas and high voltage. A gas mixture of pentane-CO₂ in the appropriate proportions was prepared and delivered to each sTGC with a gas system designed and made at McGill University [60]. Since pentane is flammable, the gas system was designed with safety top of mind. The gas system was controlled by a slow control program, also custom made [60]. To prepare the quadruplets for operation, CO₂ was flushed through them overnight to remove potential impurities within each chamber’s gas volume. Then, the equivalent of approximately five sTGC gas volumes of the pentane-CO₂ mixture was flushed through to ensure a uniform gas mixture inside the sTGCs; the procedure takes approximately four hours. High voltage was provided by commercial CAEN high voltage boards [60].

5.3 Data acquisition

Each sTGC electrode was connected to a channel on a prototype ASIC¹ on the front-end electronics, attached to the adaptor boards on each layer of a quadruplet. Each ASIC features 64 charge amplifiers with selectable gain and input signal polarities, which output the digitized amplitude of the signal at peak for channels above a pre-defined threshold. Thresholds were estimated [62] by optimizing the efficiency of detecting muons while minimizing noise, and further manually tuned in the configuration/readout software before the start of data acquisition for each quadruplet. The signal from the capacitively-coupled strip electrodes has positive polarity and is read out with a gain of one. For each trigger, the signal peak amplitude of all channels above threshold was recorded as an event and stored in a binary file. The readout of strips made use of a special feature of the custom ASIC, the so-called “neighbour triggering” function where signals on channels adjacent to those above threshold are also read out.

The quadruplets were held at 3.1 kV for approximately two hours to collect data from approximately 1 million muon triggers.

¹A custom Application Specific Integrated Circuit (ASIC) named VMM3 [61], designed for the readout of signals from the micromegas and sTGCs of the NSWs.

5.4 Data preparation

5.4.1 Data quality cuts on electrode hits

Corrupted data, if any, is removed while the raw data is being recorded in a binary file. After data taking is completed, the raw data is decoded and the electronics channels are mapped to physical readout electrodes of the quadruplet. The result of this data preparation step is stored in a ROOT [63] tree data format.

A hit is defined as a signal recorded from a channel that is above threshold or, in the case of strips, neighbour triggered. In addition to hits from muons, the quadruplets record noise from the electronics and δ -rays (electrons liberated with sufficient energy to escape a significant distance away from the primary radiation and produce further ionization). Therefore, selection cuts are applied to reduce the number of hits that do not originate from muons. Readout strips located at the very edge of the cathode board tend to have higher electronic noise. As a result, all strip hits on a layer where a hit is present on the strips at either edge of the quadruplet are removed from the analysis. A default pedestal value is subtracted from the recorded signal peak amplitude of each electrode for a more realistic estimate of the signal amplitude. Also, events that only have hits on pad electrodes (no strips or wires) are removed from the analysis since these hits are likely from electronic noise, which is higher on the pad readout channels due to their large area.

5.4.2 Clustering and tracking

For events passing the quality selection cuts defined in Section 5.4.1, the x - and y -coordinates of the ionization avalanche on each layer are extracted from the signal on the wires and strips respectively for each event, as shown schematically in Figure 5.2. In this work, x is defined as the coordinate perpendicular to the wires and y is defined as the coordinate perpendicular to the strips. The z -coordinate is perpendicular to the sTGC surface.

The x -coordinate of the muon position is taken as the center of the wire group with the maximum peak signal amplitude, since the wire groups' pitch (36 mm) is larger than the typical extent of the ionization charge generated inside a sTGC. Assuming that the true x -position of the hit is sampled from a uniform distribution over the width of the wire group, the uncertainty in the x -position is approximately $\frac{36}{\sqrt{12}}$ mm = 10 mm [64].

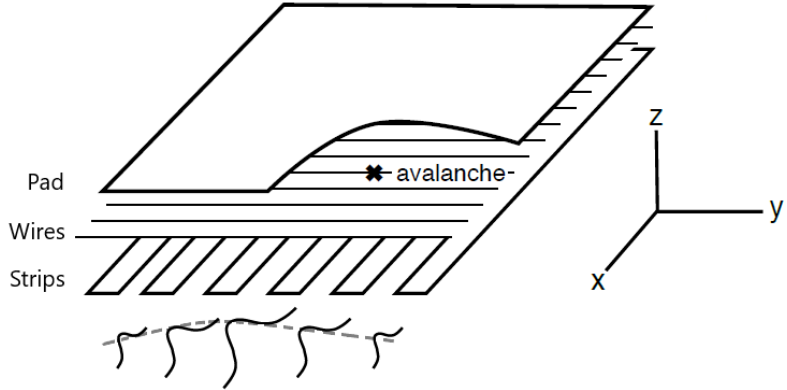


Figure 5.2: Schematic diagram representing the three types of electrodes in a sTGC detector. The position of the ionization avalanche is extracted from the wires and strips that picked up the avalanche signal. The signals on individual strips are sketched. Clustering is the process by which a Gaussian function (represented by the grey dashed line) is fitted to the distribution of the signal amplitude on individual contiguous strips; a sample cluster is shown in Figure 5.3. In this work, the $x(y)$ -coordinate will always refer to the coordinate perpendicular to the wires (strips). The z -coordinate is perpendicular to the sTGC surface [58, 56].

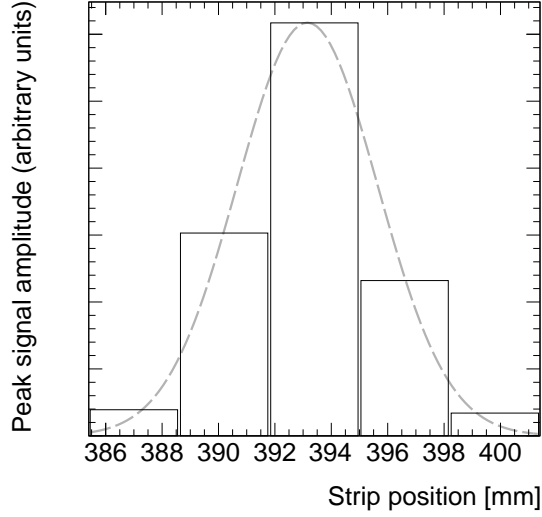


Figure 5.3: A sample cluster resulting from signal recorded on a group of contiguous strips after the passing of a muon. The grey dashed line represents the result of a fit to a Gaussian distribution.

The y -coordinate of the muon's position is taken as the Gaussian mean of the peak signal amplitude distribution across a group of contiguous strips that registered hits. The process of grouping contiguous strip hits on a layer is called clustering, and the resulting group is called a cluster. Figure 5.2 sketches the clustering process and a sample cluster is shown in Figure 5.3. The data acquisition system recorded the identification number of the strip electrode that was hit and in the clustering process the position of the center of the strip electrode is calculated based on the nominal quadruplet geometry. Typically, clusters are built of 3-5 strips. The thickness of the graphite coating over the cathode boards determined how many strips picked up the ionization image charge. Larger clusters can often originate from δ -rays since they spread the ionization charge over a larger area.

Events are removed from further analysis if there are two reconstructed clusters on one sTGC, since some hits could be from electronic noise or a simultaneous second muon traversing the chamber. Clusters are rejected if the cluster size is less than three strips (which should not happen for real events thanks to neighbour triggering), and if the cluster size is greater than 25. After all quality selection cuts are applied on hits and clusters, approximately half of the events recorded remain.

The uncertainty on the reconstructed cluster position is assessed by comparing the difference between Gaussian means obtained using two different algorithms. As shown in Appendix A, the difference between the means from the two algorithms considered is found to be approximately 60 μm on average, larger than the statistical uncertainty on the Gaussian mean obtained from the cluster fit. Therefore, an uncertainty of 60 μm is assigned to the reconstructed y -coordinate of a muon.

The reconstructed x and y coordinates on each quadruplet layer are used to reconstruct a straight track, independently, in the x - z and y - z planes. Tracks are reconstructed using muon coordinates for every possible pair of two sTGC layers. For example, if an event has muon coordinates reconstructed on all four layers, a total of six track segments in the x - z plane and six track segments in the y - z plane will be reconstructed. The uncertainty in the interpolated or extrapolated track y -(x -)position comes from propagating the 60 μm (10 mm) cluster position uncertainty. The maximum uncertainty in the track y -(x -)positions is 0.4 mm (40 mm) in the case with the worst extrapolation lever arm.

5.5 Relative local offsets

The offset of a strip from its nominal position can be modeled as a passive transformation. The *local offset* is defined as the shift in the strip pattern with respect to nominal geometry in a specific area of the sTGC. Local offsets systematically change the set of strips nearest

to muons passing through an area. The data preparation software assumes that strips are in their nominal positions, so the recorded y -coordinate of the muon on layer i , y_i , is shifted opposite to the layer's local offset, $d_{local,i}$, by

$$y_i = y_{nom,i} - d_{local,i}, \quad (5.1)$$

where $y_{nom,i}$ is the position of the muon that would have been recorded on layer i if there was no local offset. Equation 5.1 ignores other factors that affect the cluster position, like position resolution. With cosmics data, there was no external reference to measure $y_{nom,i}$ and the local offset is unknown. Therefore, only *relative* local offsets can be measured.

To measure relative local offsets, two of the four sTGC layers are chosen to provide a reference coordinate system. Relative local offsets are calculated with respect to the two reference or fixed layers. The hits on the two fixed layers were used to create tracks that can be interpolated or extrapolated (polated) to the other two layers. The set of two fixed layers and the layer polated to are referred to as a tracking combination. The residual of track i , Δ_i , is defined as,

$$\Delta_i = y_i - y_{track,i}, \quad (5.2)$$

where $y_{track,i}$ is the polated track position on the sTGC layer the residual is measured on. Track residuals are affected by the local offset in the area of each layer's hit. As an example, in Figure 5.4, the residual on layer 2 perhaps indicates that layer 2 is offset with respect to layers 1 and 4 in the area of the track. Of course, a single track residual says nothing of the real relative local offset because of the limited spatial resolution of the detectors and fake tracks caused by noise or delta rays. However, the mean of residuals for all tracks in a region of interest will be shifted systematically by the local offsets between layers [58]. For a quadruplet with nominal geometry, the mean of residuals should be zero in all regions and for all reference frames, unlike the example regions in Figure 5.5. The value of the mean of residuals is a measure of the relative local offset of the layer with respect to the two fixed layers used to reconstruct the muon track. The sign convention is such that the mean of residuals is opposite to the relative local offset.

To study the relative local offsets, residual distributions across each strip layer of a quadruplet for all possible tracking combinations are assembled and fitted. As expected, the residual distributions are wider for tracking combinations where the extrapolation lever arm is largest, as in the example distributions shown in Figure 5.5. In general, residual means from distributions of residuals with geometrically less favourable tracking combinations have larger statistical and systematic uncertainties. The bin size of 200 μm for the distributions shown in Figure 5.5 was chosen based on the order of the uncertainty on residuals calculated from tracks on layer 4 (1) built from hits on layers 1 and 2 (3 and 4) given a cluster y -coordinate

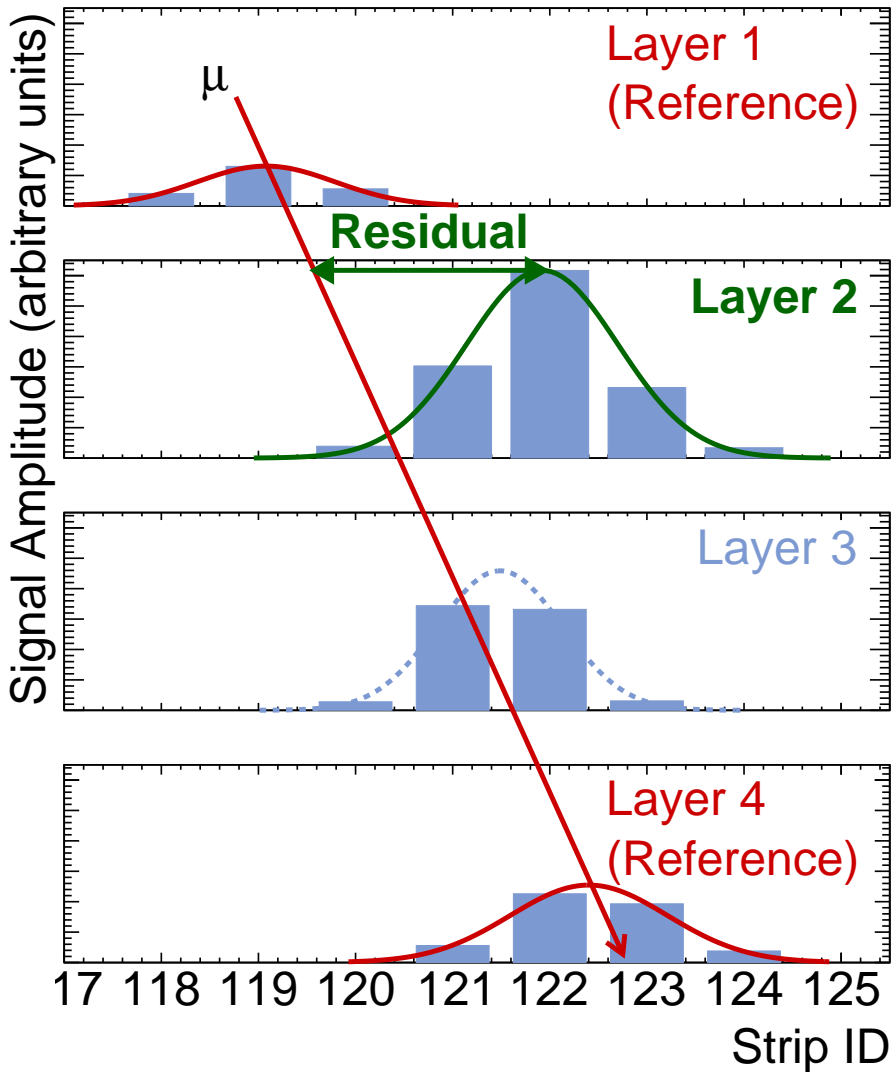
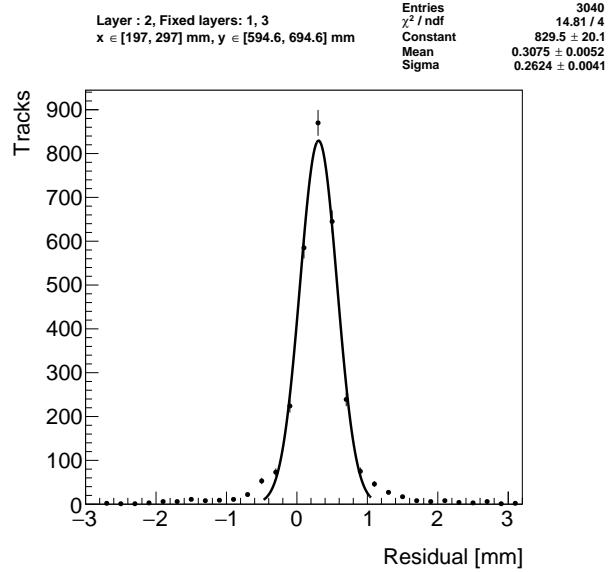
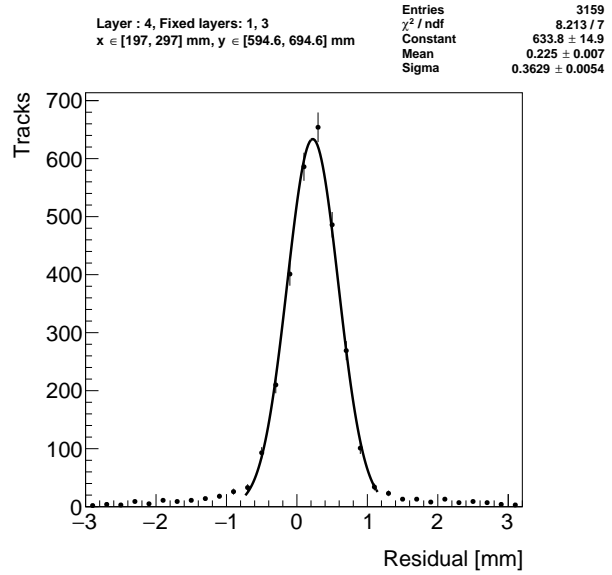


Figure 5.4: Representation of a muon event recorded by an sTGC quadruplet. The charge clusters measured using strip electrodes are fit with a Gaussian distribution and the fitted mean is taken as the reconstructed muon position. A track is built from the chosen reference layers, 1 and 4, and the track residual is calculated on layer 2. The clusters come from a real muon, but their positions were modified to highlight the non-zero value of the residual on layer 2.



(a) Tracks on layer 2, reference layers 1 and 3.



(b) Tracks on layer 4, reference layers 1 and 3.

Figure 5.5: Residual distribution in the region $x \in [197, 297]$ mm, $y \in [594.6, 694.6]$ mm (100 mm by 100 mm area) for two different tracking combinations. Data from quadruplet QL2.P.11.

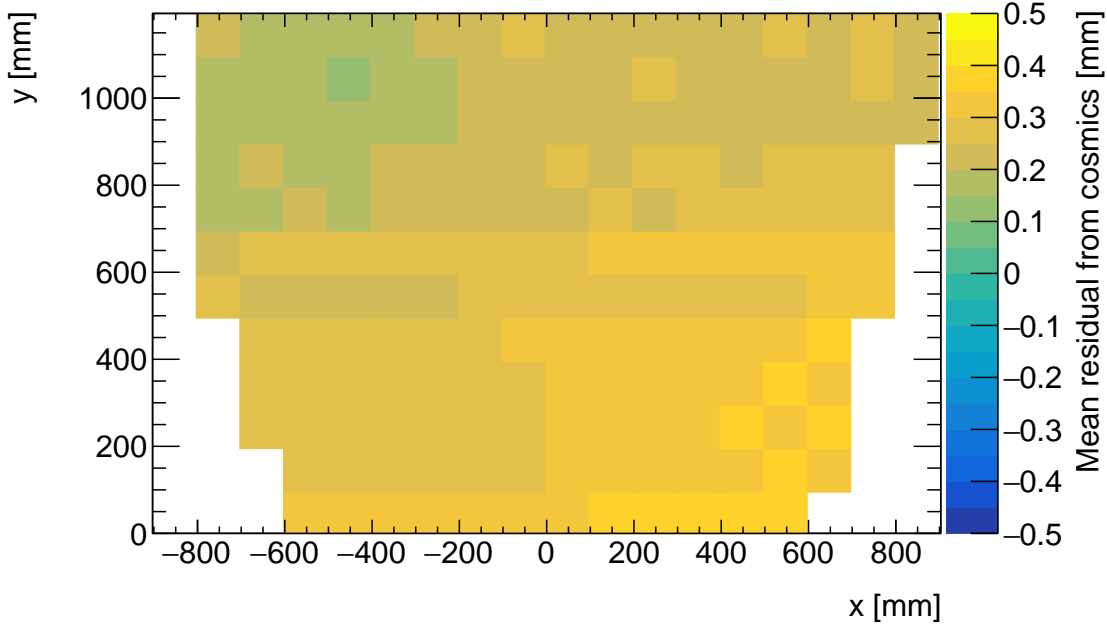
uncertainty of $60\text{ }\mu\text{m}$ (discussed in Section 5.4.2 and Appendix A), since these tracks yield residuals with the largest uncertainties.

A Gaussian fit is used to extract the mean of the residual distributions. The residual distributions are actually better modeled by a double Gaussian distribution, which better captures the distribution tails in Figure 5.5. However, a study described in Appendix C.1 found that a fit to a single Gaussian function in the core of the distribution is sufficient to reconstruct the mean of the distribution.

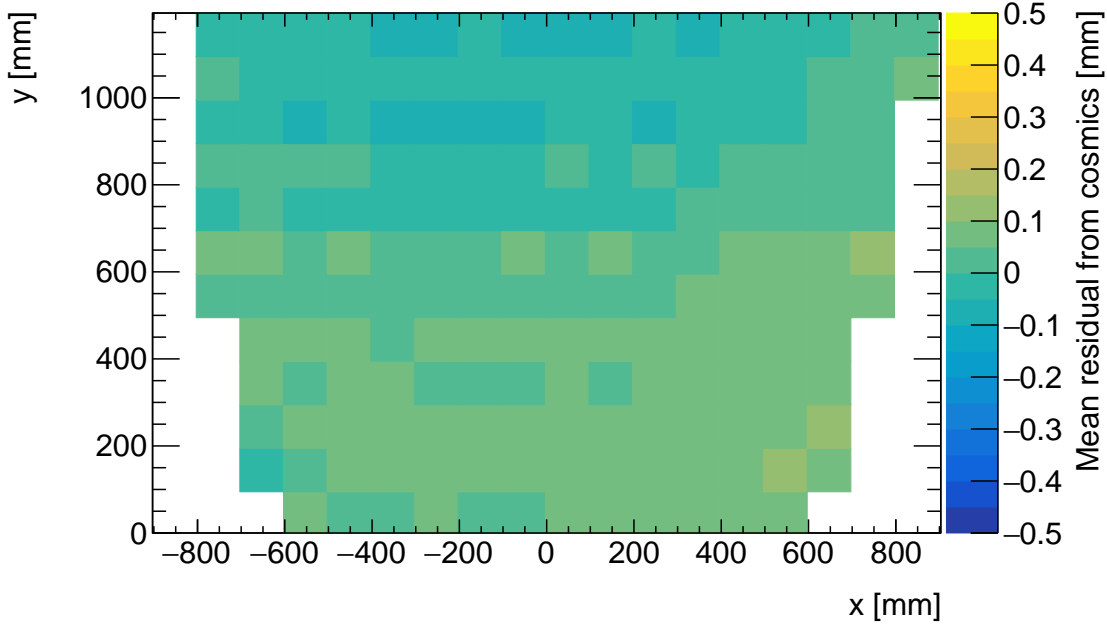
The area of the region of interest where tracks residuals were included in the residual distribution was 100 mm by 100 mm. The size balanced the number of tracks falling in the region of interest to give a small statistical uncertainty on the fitted mean while being smaller than the order on which local offsets were expected to change significantly. “Significantly” was defined as $100\text{ }\mu\text{m}$, the required position resolution of the sTGCs and the precision to which strip positions should be known. The distance over which local offsets are expected to change significantly can be estimated using a simple alignment model. Assuming the strips of a layer have been displaced uniformly from their nominal positions by a global offset and rotation, the distance in x that a large but possible rotation of 1 mrad changes the local offset by $100\text{ }\mu\text{m}$ is 100 mm.

The means of residuals are plotted across each sTGC layer for every possible tracking combination to get a picture of the how the relative local offsets change as a function of position over the layer’s surface. Figure 5.6 shows the mean of residuals on layer 2 calculated with layers 1 and 3 as reference for two different quadruplets, referred to as QL2.P.11 and QL2.P.8. In Figure 5.6a, the Gaussian mean of the residual distribution in Figure 5.5a is the entry in the bin defined by the boundaries $x \in [197, 297]\text{ mm}$, $y \in [594.6, 694.6]\text{ mm}$.

Many of the residual means are non-zero and change smoothly over layer 2, indicating that there are relative local offsets stemming from global misalignments between the strip patterns of different sTGC layers in both quadruplets. Given that the residual mean changes with x in Figure 5.6a, quadruplet QL2.P.11 likely has a rotation of layer 2 with respect to layers 1 and 3, combined with an offset of the entire layer. The residual means are smaller in Figure 5.6b indicating that quadruplet QL2.P.8 is less misaligned overall than QL2.P.11; however, the relative local offsets range between $\pm 200\text{ }\mu\text{m}$ so they are significant enough to warrant a correction so the quadruplet can achieve the required track angular resolution in the NSW.



(a) Mean of track residuals on layer 2, obtained using layers 1 and 3 as reference, for QL2.P.11.



(b) Mean of track residuals on layer 2, obtained using layers 1 and 3 as reference, for QL2.P.8.

Figure 5.6: Mean of residuals in each 100 mm by 100 mm bin over the area of sTGC layer 2 for quadruplets QL2.P.11 and QL2.P.8. The entry in $x \in [197, 297]$ mm, $y \in [594.6, 694.6]$ mm of Figure 5.6a corresponds to the fitted Gaussian mean in Figures 5.5a. The mean of residuals has the same value and opposite sign to the relative local offset of layer 2 with respect to the reference frame defined by layers 1 and 3.

5.6 Systematic uncertainty

The statistical uncertainty on the local residual means was typically around 10 - 20 μm , and Appendix B shows that the analysis is not statistically limited by the number of triggers collected for each quadruplet. Systematic uncertainties were found to be larger than the statistical uncertainty on the residual means.

Several analysis choices had some degree of impact on the fitted means of local track residual distributions. To study the impacts, the residual means were calculated in different ways and distributions of the differences made. The complete studies are shown in Appendix C. The root-mean-square (RMS) of the residual mean difference distributions were used to quantify the impact of the different analysis choices as systematic uncertainties on the residual means. The following analysis choices are considered:

- The impact of performing a single or double Gaussian fit on the track residual distributions is studied. As shown in Appendix C.1, the difference between fitting the track residual distribution with a single or double Gaussian function varies between 10 and 30 μm from the most to least geometrically favourable tracking combinations.
- The impact of the operating voltage used during data taking is investigated. Cosmic muon data was recorded at 2.9 kV and 3.1 kV. As described in Appendix C.2, an uncertainty between 10-40 μm is assigned to the different tracking combinations.
- The impact of using different Gaussian fitting algorithms used to reconstruct the position of a charge cluster was considered. Clusters are fit with the Minuit2 [65] and Guo's method [66]. As shown in Appendix C.3, the resulting difference in residual means is between 10-30 μm from the most to least geometrically favourable tracking combinations.
- The impact of correcting reconstructed cluster positions for differential non-linearity (DNL) is studied. DNL is fully described in Appendix C.4. It is a bias in the reconstructed cluster position that comes from discretely sampling a continuous distribution, in this case the charge distribution [67, 58, 6]. The difference between residual means is compared with and without correcting the reconstructed cluster positions. Appendix C.4 shows that the impact of the correction is smaller than 10 μm for all tracking combinations, which is almost negligible.

A summary of the systematic uncertainties assigned to the local means of residuals for each tracking combination is given in Table 5.1. The RMS of the distributions of residual mean differences of geometrically similar tracking combinations are averaged and the average value

Tracking geometry	Residual distribution fit function (C.1)	Cosmics data collection voltage (C.2)	Cluster fit algorithm (C.3)	Apply DNL correction or not (C.4)	Total
Similar to layer 3, fixed layers 1, 2	0.01 mm	0.04 mm	0.02 mm	0.01 mm	0.05 mm
Similar to layer 4, fixed layers 1, 2	0.03 mm	0.01 mm	0.03 mm	0.01 mm	0.10 mm
Similar to layer 2, fixed layers 1, 3	0.01 mm	0.02 mm	0.01 mm	0.000 mm	0.03 mm
Similar to layer 4, fixed layers 1, 3	0.01 mm	0.04 mm	0.01 mm	0.01 mm	0.04 mm
Similar to layer 2, fixed layers 1, 4	0.01 mm	0.04 mm	0.01 mm	0.01 mm	0.04 mm

Table 5.1: Systematic uncertainties assigned for each analysis option per tracking combination. Details can be found in Appendix C. The total systematic uncertainty is obtained by summing in quadrature all the individual systematic uncertainties.

is taken as the systematic uncertainty for those tracking combinations. An example of a geometrically similar pair of tracking combinations is fixing layers 1 and 2 and extrapolating to layer 3 or fixing layers 2 and 3 and extrapolating to layer 4; geometrically similar combinations have the same polation lever arm. The total systematic uncertainty is obtained by summing in quadrature all the different sources of systematic uncertainty. The uncertainty in each mean of residuals is obtained by summing in quadrature the statistical uncertainty in the mean of residuals and the appropriate systematic uncertainty for the tracking combination used to calculate the mean of residuals.

5.7 Discussion

The total uncertainty in the residual means, and hence the relative local offsets, is typically less than the design sTGC position resolution of $\sim 100 \mu\text{m}$ [5]. Therefore, the residual means are relevant input for alignment studies.

The relative local offsets calculated from the means of residual distributions over the surface of an sTGC layer for all tracking combinations provide a complete picture of the relative alignment between sTGC layers in a quadruplet module. In fact, cosmic muon testing is the only characterization technique where the entire surface of quadruplet layers can be probed since muons hits are distributed almost uniformly; the CMM [7] and x-ray methods [8] depend on measurements at reference points, and test beams only have a limited beam spot to work with [6]. By looking at 2D-histograms of residual means like Figure 5.6 for all tracking combinations, it is easy to identify quadruplets that suffer large relative misalignment since many residual means differ significantly from zero. Moreover, the pattern in the residual means can be used to motivate a physical interpretation of misalignments. The residual means can be used as a reference, cross check, or input to other alignment studies.

Relative local offsets cannot be used to position strips in the absolute ATLAS coordinate system because there is no external reference to measure positions on all layers with respect to. The lack of an external absolute reference frame means that there is not enough information to unfold relative local offsets into absolute local offsets (with respect to the nominal quadruplet geometry). As an example, assuming that the residual on layer 2 in Figure 5.4 is representative of the absolute value of the relative local offset, the residual on layer 2 could be caused by the strips on layer 2 being misaligned from nominal, but it could also be caused by strips on layers 1 and 4 being offset from nominal while the strips on layer 2 are in their nominal positions! Any number of combinations of local offsets on layers 1, 2 and 4 could produce the residual on layer 2. Absolute local offsets must be calculated using another method: the x-ray method.

Chapter 6

Using x-rays to measure relative strip position offsets

This chapter describes the analysis of x-ray data to measure relative local strip position offsets, which can be compared with results obtained using cosmic data. The reader is referred to the paper describing the x-ray method [8]. Some minor changes to the experimental setup have been made since the paper was written. The experimental setup described here is current and was used to collect the data presented in this thesis.

6.1 Experimental setup

The x-ray tests were performed after the quadruplets arrived at CERN, were assembled into wedges, and the alignment platforms installed. An x-ray gun was attached to one of the alignment platforms glued to the surface of the wedge and the x-ray beam profile was recorded by the strip electrodes.

The sTGC wedges were installed on carts that could rotate their surface to a horizontal position. A mounting platform was installed on top of the alignment platform using a three-ball mount. The x-ray gun used was an Amptek Mini-X tube [68]. The x-ray gun was placed in a brass holder with built-in 2 mm collimator and 280 μm copper filter. The holder was mounted on one of five positions on the mounting platform, as shown in Figure 6.1. The x-ray gun positions were chosen to avoid wire support structures in the sTGCs that reduce hit efficiency [58] and boundaries between sets of strips read out by two different ASICs that could each have different thresholds.

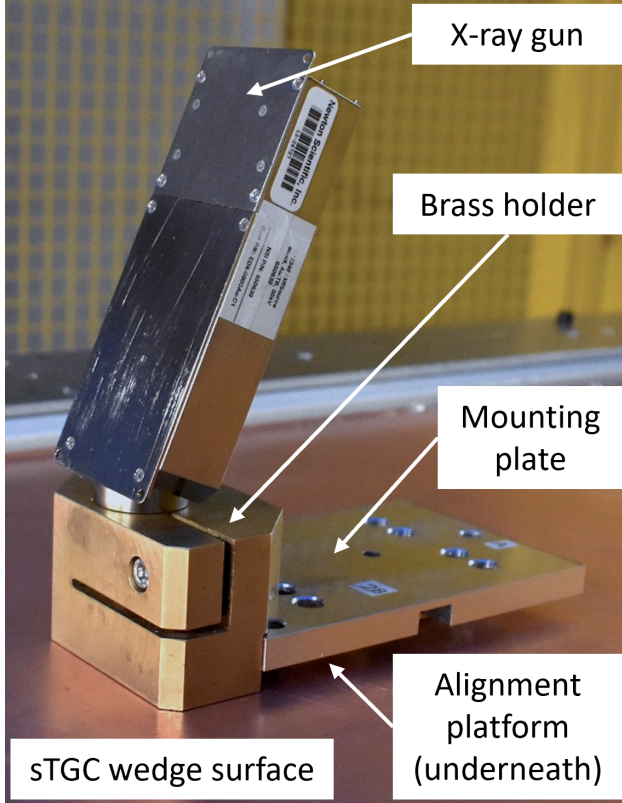


Figure 6.1: The x-ray gun mounted to an alignment platform on the surface of a sTGC wedge. Adapted from [8].

As with cosmics data collection, each sTGC also needed gas and high voltage to operate. Each sTGC layer was operated at 2.925 kV with high voltage from a NIM module. The sTGC gas volumes were flushed with CO₂ before and during data collection. The sTGCs were not operated using the nominal pentane-CO₂ gas mixture due to constraints in its availability based on safety concerns. The sTGC efficiency is significantly lower when operated with only CO₂.

The gun produced x-rays with energies under 40 keV with peaks in the 7-15 keV range. Peaks in the 0-30 keV range were filtered out by the copper filter and the copper of the sTGCs. The x-rays mostly interacted with the sTGC wedge's copper electrodes and gold-plated tungsten wires via the photoelectric effect. The resulting photoelectrons that enter the gas volume caused ionization avalanches which were picked up by the readout strips.

6.2 Data acquisition

A different version of the same front end electronics, but the same ASIC, as used in cosmics testing were used for the x-ray testing to measure the peak signal amplitude. Data was collected for two minutes per gun position with random triggers. A trigger recorded all signals above threshold. Pad and wire data was not recorded.

6.3 Data preparation

Following a similar approach to the cosmics data analysis described in Chapter 5, a default pedestal is subtracted from the signal peak amplitude on each electrode.

Clusters are defined as groups of contiguous strip hits recorded within 75 ns. The distribution of peak signal amplitude from continuous strip hits is fitted with a Gaussian function, and the mean of the fitted Gaussian is taken as the cluster position. Cluster positions are corrected for differential non linearity (or DNL, see definition in Appendix C.4). Although the impact of the DNL correction on the reconstructed cluster means is small, it is important to improve the spatial resolution of the sTGC strip layer. Only clusters composed of hits on 3-5 strips are used in the x-ray analysis. Clusters with signal on more than five strips are cut because they were most likely caused by photoelectrons ejected with enough energy to cause more primary ionization and subsequent avalanches as δ -rays.

The x-ray analysis diverges entirely from the cosmics analysis algorithm here because the ionization from x-rays does not originate from one charged particle traversing all layers of a sTGC quadruplet, so there is no track to rebuild. Rather, ionization avalanches [54] are generated by photoelectrons liberated from the metals of the sTGCs, which only travel through one gas volume and are produced at all angles. Instead of reconstructing a straight line trajectory through multiple sTGC layers, the cluster position distribution on each sTGC layer is used to reconstruct the beam profile. A typical x-ray beam profile is shown in Figure 6.2.

6.4 Measuring local offsets

The fitted Gaussian mean of the cluster position distribution is taken as the reconstructed center of the x-ray beam profile on each sTGC layer. The reconstructed center is compared to the expected beam profile center, calculated in two steps. First, the position of the alignment platform with respect to the brass inserts and the nominal position of the strips under the

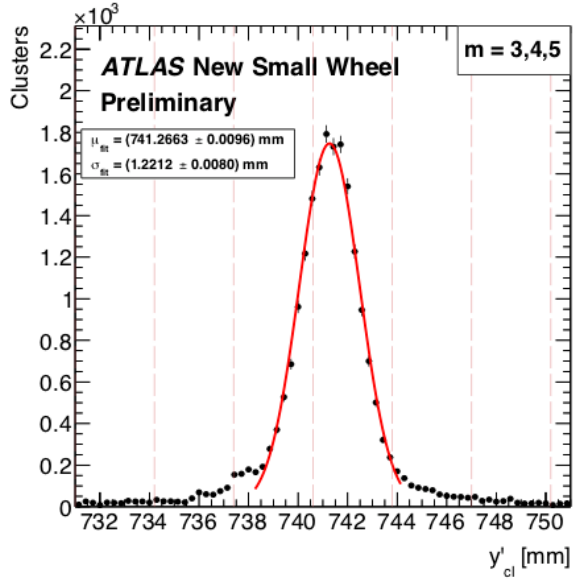


Figure 6.2: An example distribution of x-ray cluster mean positions after the analysis selection cuts and DNL corrections are applied. The strip cluster multiplicity, m , was limited to 3, 4 or 5. The red curve is a Gaussian fit of the distribution and the pink dashed lines denote the edges of the strips [8].

gun position with respect to the brass inserts are used to calculate the expected beam profile center assuming a nominal quadruplet geometry. Second, the expected beam profile center is corrected for the geometry of the brass holder, the positioning and angle of the alignment platforms, and the beam angle. The difference between the expected and reconstructed beam profile centers is a measure of the local offset of the strip electrode pattern. Applying the logic of Equation 5.1 to the beam profile, the Gaussian mean of cluster positions on the given layer acts as the recorded position, y_i , the expected center is $y_{nom,i}$ and the local offset is $d_{local,i}$ as before, where i denotes the layer. Since the position of the alignment platforms will be monitored continuously by the alignment system in ATLAS [5], the position of the strips that should have been at the x-ray gun position are shifted by $d_{local,i}$ and so their absolute positions in the ATLAS coordinate system are known for every position where x-ray data was recorded. Therefore, the x-ray local offsets can be used to measure the position of some strips in the ATLAS coordinate system, as is required for the triggering and precision tracking goals of the NSWs as discussed in Chapter 4.

Studies of systematic effects on the measured beam profile centers lead the x-ray working group to accept an uncertainty of 120 μm on the beam profile centers. The largest uncertainty

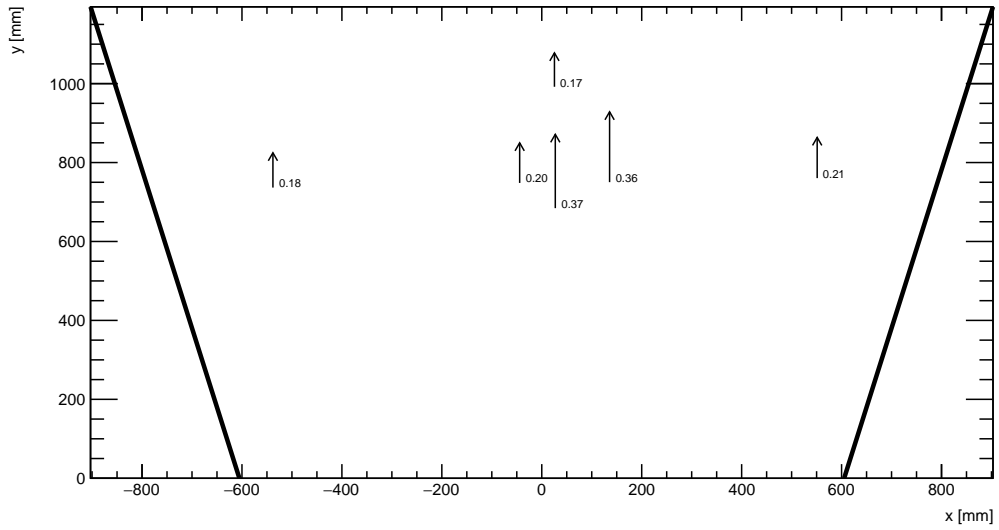
comes from the effect of the gun angle, which proved difficult to measure and correct for. The details and results of the systematics studies have not been published externally.

The absolute local strip offsets measured using the method described above are not presented here as the author did not conduct this work. However, the author used the *absolute* local offsets to calculate *relative* local offsets that can be compared to the relative local offsets measured using cosmic muon data.

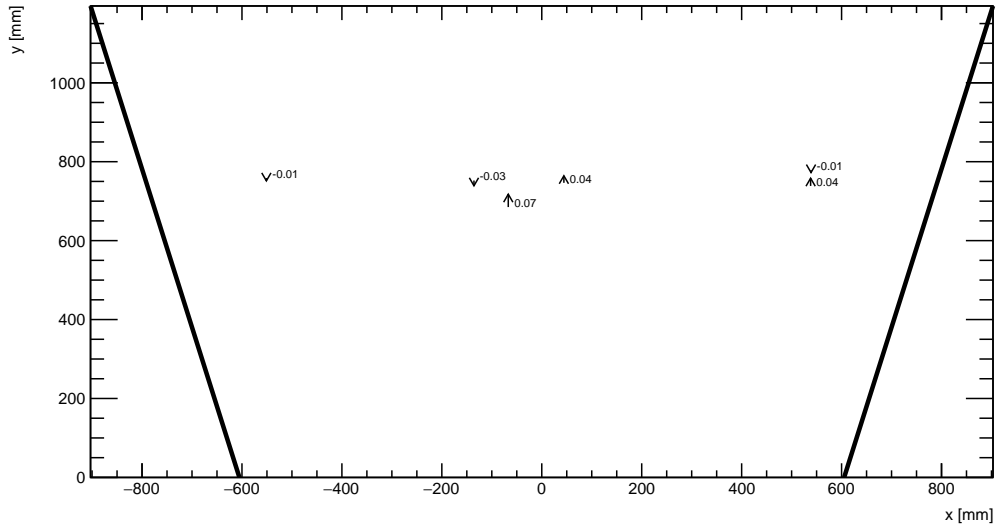
6.5 Measuring relative local offsets

The novelty of the x-ray method and the uncertainty in the x-ray local strip position offsets, which are greater than the precision to within which the position of the strips would ideally be known, means that the x-ray local offsets should be validated by an independent method. Absolute local offsets measured using x-ray data and relative local offsets measured using cosmics data cannot be compared directly because they are not defined with respect to the same coordinate system: x-ray absolute local offsets are measured in the ATLAS coordinate system while cosmics relative local offsets are defined with respect to a reference frame established by two sTGC layers in a quadruplet. The following describes the method used to calculate relative local strip position offsets from the x-ray local offsets that can be compared to the cosmics relative strip position offsets.

Given that the measured x-ray beam profile centers are systematically affected by local strip position offsets in the same way as the means of the cosmic ray track residual distributions, the x-ray beam profile centers on each sTGC layer are used to reconstruct a straight line in the y - z plane using the beam profile centers on two sTGC layers chosen as reference, in a manner similar to the track reconstruction performed with cosmic muon data. A residual is calculated as the difference between the beam profile center on the layer of interest and the polated straight line fitted from two sTGC layers taken as a reference. The beam profile center on the layer of interest acts as y_i and the polated track position acts as $y_{track,i}$ in Equation 5.2. As with the means of cosmic track residual distributions, the sign convention is such that the x-ray residual is opposite in sign to the relative local offset of the layer of interest with respect to the two fixed layers.



(a) X-ray residuals on quadruplet QL2.P.11 layer 2 obtained using reference layers 1 and 3.



(b) X-ray residuals on quadruplet QL2.P.8 layer 2 obtained using reference layers 1 and 3.

Figure 6.3: The x-ray residuals on sTGC layer 2 calculated with respect to the beam profile centers on sTGC layers 1 and 3 for quadruplet QL2.P.11 (a) and QL2.P.8 (b). The arrows originate from the expected position of the beam profile center assuming a nominal geometry. The lengths of the arrows are 500 times the value of the x-ray residuals, scaled for visibility. The value of the x-ray residuals are annotated in millimeters and have an uncertainty of ± 0.15 mm.

For each x-ray survey position, the x-ray residuals were calculated for all possible pairs of sTGC layers taken as reference and each sTGC layer the straight line could be polated to, as was done for cosmic muon tracks. Calculating a residual required x-ray beam profiles on at least three layers. Figure 6.3 shows the x-ray residual values on sTGC layer 2 with respect to reference layers 1 and 3 for sTGC quadruplet modules QL2.P.11 and QL2.P.8. For module QL2.P.11, a negative relative local offset is measured at all x-ray survey points, indicating a global translation of sTGC layer 2 with respect to layers 1 and 3.

The uncertainty on the x-ray residuals is obtained by propagating the uncertainty on the reconstructed x-ray beam profile centers ($120\text{ }\mu\text{m}$) through the polation. The uncertainty on the x-ray residuals ranges from $150\text{ }\mu\text{m}$ to $400\text{ }\mu\text{m}$ from the most to least geometrically-favourable tracking combination. There is no discernible pattern of misalignment revealed by the x-ray residuals on QL2.P.8 because they have absolute values smaller than the uncertainty on the x-ray residuals ($150\text{ }\mu\text{m}$).

The relative local offsets calculated using cosmics data and x-ray data will be compared in the next chapter.

Chapter 7

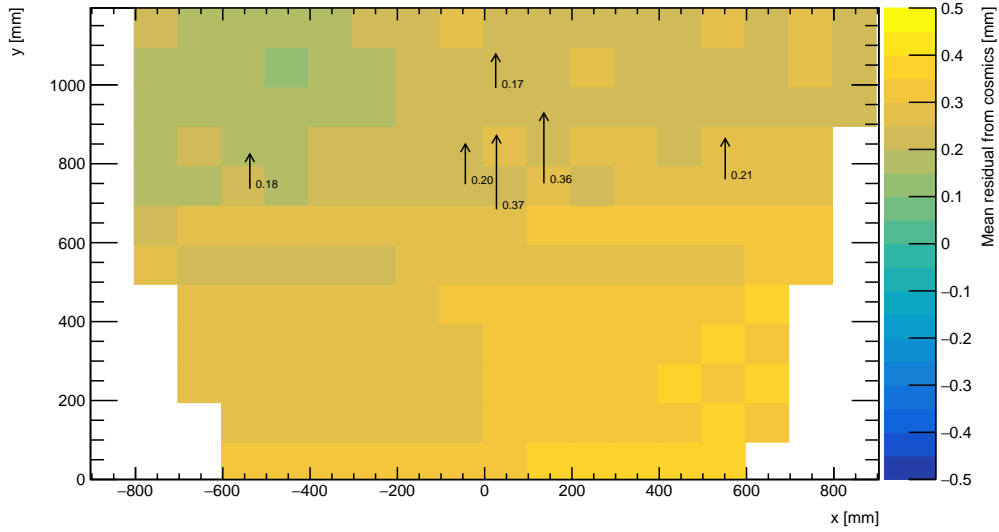
Comparing cosmic muon and x-ray relative strip position offsets

The goal of the work presented in this thesis is to validate the local strip position offsets measured with x-ray data with results obtained using cosmic ray data. The challenge was that the x-ray dataset provided absolute local offsets measured in the ATLAS coordinate system while the cosmics dataset provided relative local offsets measured with respect to a reference frame defined by two of four sTGC layers in a quadruplet – which could not be compared directly. To address the challenge, the x-ray local offsets were used to calculate relative local offsets. Relative local offsets on each sTGC layer obtained with x-ray and cosmics data calculated using the same two sTGC reference layers are compared for each area where x-ray data is available. The results of the comparison are presented here.

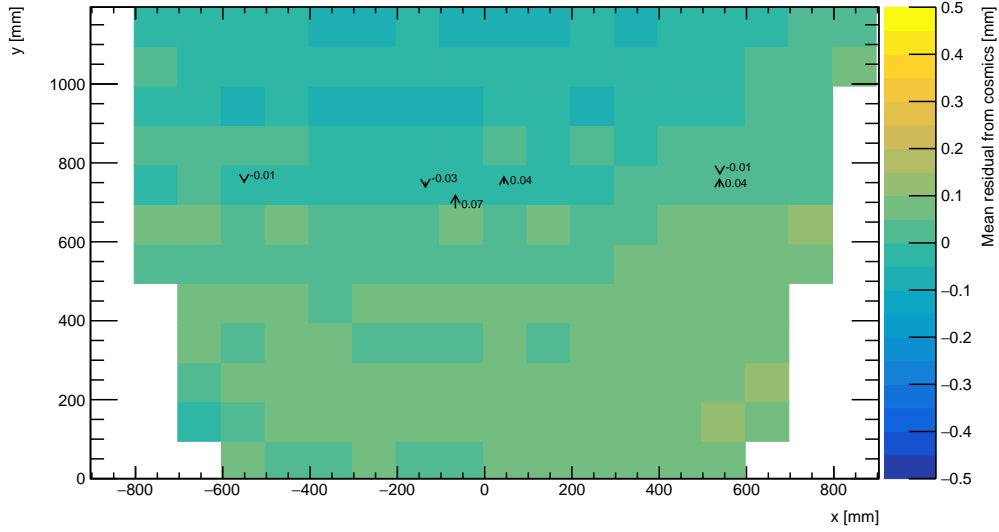
7.1 Results

Relative local offsets have the same value but opposite sign to the mean cosmics and x-ray residuals. For the remainder of this chapter, the means of cosmic track residual distributions will be referred to as mean cosmics residuals.

Mean cosmics and x-ray residuals on sTGC layer 2 calculated with reference layers 1 and 3 across the quadruplet surface are shown in Figure 7.1 for sTGC quadruplets QL2.P.11 and QL2.P.8. Figure 7.1 is a superposition of Figures 5.6 and 6.3.



(a) Mean cosmics and x-ray residuals on sTGC layer 2 of quadruplet QL2.P.11 obtained using reference layers 1 and 3.



(b) Means cosmics and x-ray residuals on sTGC layer 2 of quadruplet QL2.P.8 obtained using reference layers 1 and 3.

Figure 7.1: The mean cosmics residuals are shown using colour. The x-ray residuals available at nominal gun positions are drawn as arrows and the value of the residual annotated in millimeters with uncertainty ± 0.15 mm. The length of the arrows is 500 times the value of the x-ray residual, scaled for visibility. These plots are a superposition of Figures 5.6 and 6.3.

Figure 7.1a shows that for QL2.P.11 the x-ray residuals are of the same sign and order as the mean cosmics residuals, as can be seen by comparing the annotated value of the x-ray residual to the mean cosmics residual represented in the nearest coloured bin. QL2.P.11's mean cosmics and x-ray residuals are correlated.

For QL2.P.8, Figure 7.1b shows that the x-ray residuals are of the right order compared to the mean cosmics residuals; however, the values of the x-ray residuals are within their uncertainty so the correlation is not manifest. While the x-ray residuals do not reveal a pattern in the relative local offsets across the layer's surface, the mean cosmics residuals show a structure to the relative local offsets, revealed by how they vary smoothly over the surface of sTGC layer 2.

The comparison of mean cosmics and x-ray residuals was done for several sTGC quadruplets for all possible tracking combinations. Scatter plots of the x-ray and mean cosmics residuals on QL2.P.11 and QL2.P.8 for all tracking combinations are shown in Figures 7.2 and 7.3 and reveal the degree of correlation between the datasets. In these correlation plots, each rectangle is centered on the value of a mean cosmics and x-ray residual pair calculated with a given tracking combination for every x-ray gun position where data is available. The height and width of the rectangles are the uncertainty in the mean cosmics and x-ray residuals respectively. Note that in the scatter plots, the regions of interest where cosmics tracks are included in the calculation of the mean of residuals are exactly centered on the nominal x-ray beam positions, unlike in Figure 7.1.

The fitted slope and offset in Figure 7.2 show that the two QL2.P.11 datasets are correlated. Note that fitting a line to the scatter plots was to aid the reader in identifying the degree of correlation; since each point is a comparison of two independent measurements, the line does not describe an underlying distribution. The large uncertainty on the x-ray residuals set a limit on the sensitivity of the analysis, for if the absolute value of the x-ray residuals of a quadruplet were smaller than the x-ray residual uncertainties, no conclusion about the correlation could be drawn, as is the case for layer 2 of sTGC quadruplet QL2.P.8 (Figure 7.3). This result is reflected in the small x-ray residuals shown in Figure 7.1b that do not reveal a pattern in the relative local offsets across the surface of sTGC layer 2. However, Figure 7.3 shows that the x-ray and mean cosmics residuals are clustered approximately around zero as is expected for a quadruplet with small relative misalignments between layers.

There are three patterns in the residuals on the scatter plot explained by geometry. First, for both datasets the uncertainty in the extrapolated track residuals were larger than the interpolated track residuals because of the extrapolation lever arm. For the x-ray residuals, the effect of the lever arm on the uncertainty was direct since the residual was calculated from a single straight line; for the mean cosmics residuals it is the widening of the residual

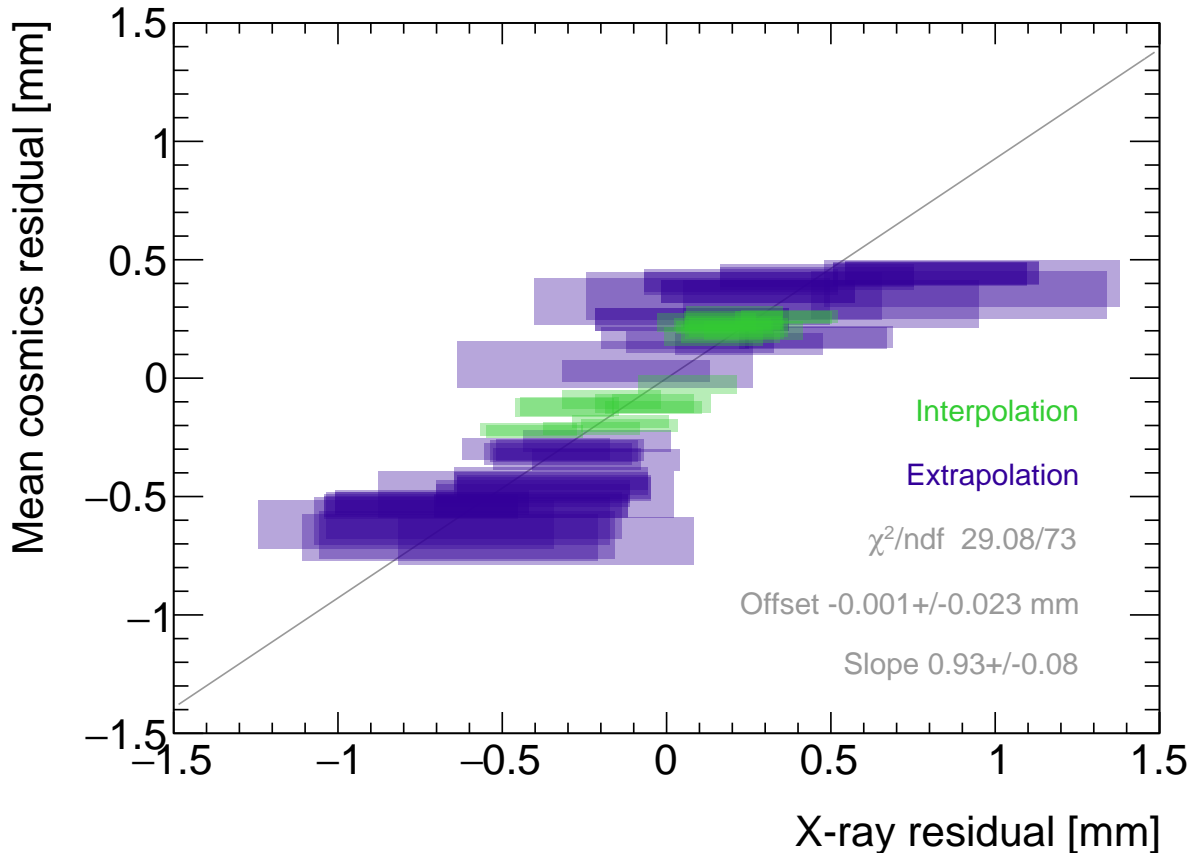


Figure 7.2: Correlation plot between x-ray and mean cosmics residuals for all tracking combinations for QL2.P.11. Each rectangle is centered on an x-ray and mean cosmics residual pair calculated at a given x-ray gun position and for a certain tracking combination. The width of the rectangles in x and y are the uncertainty in the x-ray and mean cosmics residual respectively. A printer-friendly version of this plot is available in Appendix D.

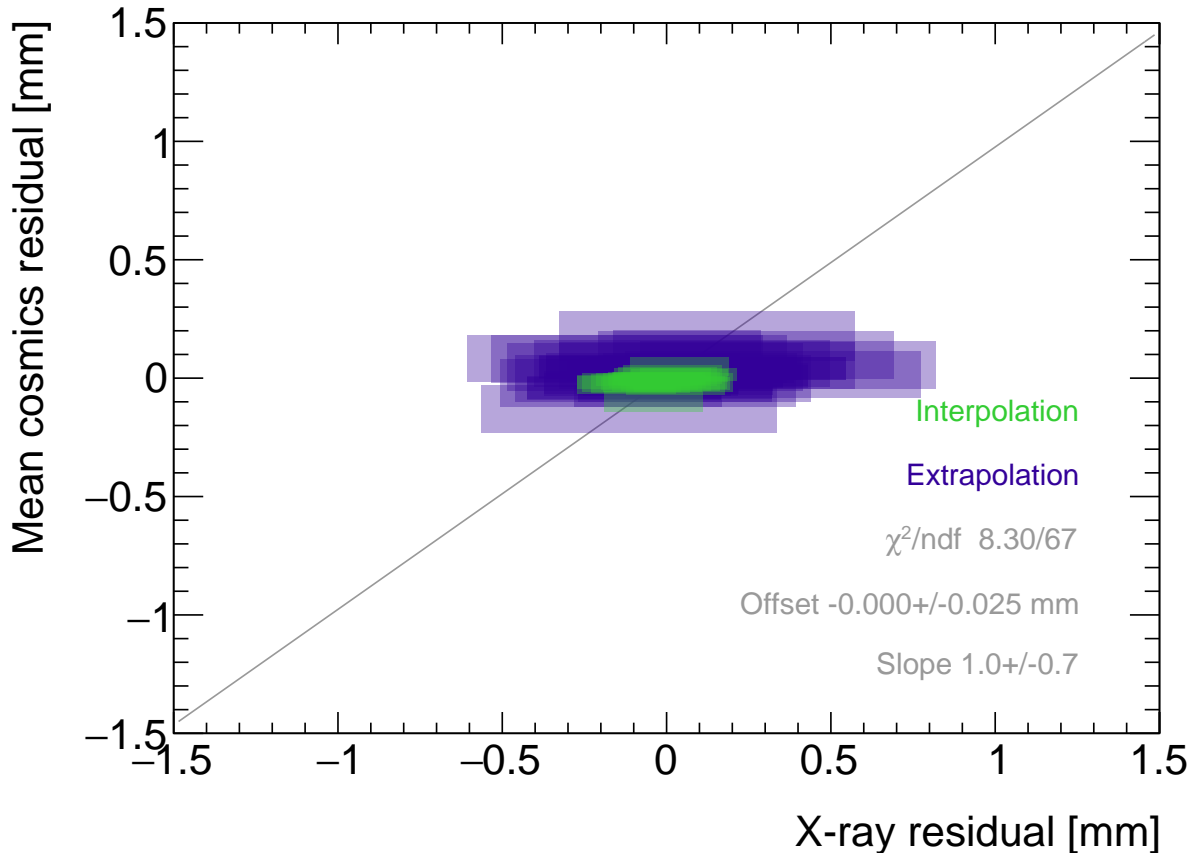


Figure 7.3: Correlation plot between x-ray and mean cosmics residuals for all tracking combinations for QL2.P.8. Each rectangle is centered on an x-ray and mean cosmics residual pair calculated at a given x-ray gun position and for a certain tracking combination. The width of the rectangles in x and y are the uncertainty in the x-ray and mean cosmics residuals respectively. A printer-friendly version of this plot is available in Appendix D.

distributions due to the extrapolation lever arm that increases the uncertainty in the fitted means of residuals. Second, residuals calculated through extrapolation tend to be larger because the extrapolation lever arm can produce more extreme values of the track position on the layer of interest. Third, the points in Figure 7.2 are geometrically correlated (e.g. they seem to be roughly mirrored around the origin). This is expected since the residuals calculated using a given set of three layers should be geometrically correlated by the local offsets on each layer (the $d_{local,i}$ on each layer as defined in Equation 5.1).

7.2 Discussion

Several sTGC quadruplets were tested for each quadruplet construction geometry built in Canada. Each quadruplet fell into one of the two categories: residuals large enough to see a correlation, or residuals too small to see a correlation. Since the x-ray and mean cosmics residuals can be used to calculate relative local offsets between the layer and the two reference layers, quadruplets with the largest relative misalignments had the largest range of residuals. The correlation plots are another easy visual way to identify quadruplets with large relative misalignments.

The most significant limit on measuring the degree of correlation between the x-ray and mean cosmics residuals is the uncertainty on the x-ray residuals, which stemmed from the systematic uncertainty of $120\text{ }\mu\text{m}$ in the x-ray beam profile centers used to construct the straight lines. For example, in Figure 7.3, if the x-ray residuals could be known to within better precision, perhaps they would be correlated with the mean cosmics residuals. The x-ray method was limited primarily by the systematic uncertainties in the relative alignment of the alignment platforms and the gun, especially the gun angle.

The analysis of a fraction of the sTGC quadruplets was limited by the availability of data. Sometimes, less than three sTGC layers in a quadruplet were surveyed for a given x-ray gun position so no residuals could be calculated. Too few x-ray residuals prevented the analysis from detecting a significant correlation with cosmics data, should it even be measurable. Often, the analysis of sTGC quadruplets of smaller sizes (placed innermost on the wheel) is limited because they have fewer alignment platforms, and hence gun positions, on their surfaces as a result of their size. The analysis is also limited to a fraction of all sTGC quadruplets built. The wedges constructed the earliest (typically small wedges) were surveyed when the x-ray method was still being designed, so a limited number of x-ray residuals can be calculated and the beam profiles were of lower quality.

Nonetheless, the comparison of x-ray and mean cosmics residuals was really to confirm the x-ray method's ability to measure local offsets with an independent dataset. The x-ray local

offsets allow the calculation of relative local offsets that have been correlated to the cosmics relative local offsets. Therefore, the analysis of quadruplets with relative local offsets large enough to detect a correlation validates the x-ray method's ability to measure local offsets.

The potential of using relative local offsets calculated from cosmics data to study relative alignment between sTGC layers stands on its own. For example, although the x-ray residuals in QL2.P.8 in Figure 7.1b do not reveal a pattern, the variation in the mean cosmics residuals do. Identifying the pattern is possible because mean cosmics residuals can be calculated across the entire sTGC layer's area and are sensitive to smaller relative local offsets since their uncertainty is significantly smaller.

7.3 Next steps

The results presented in this thesis pave the way to the further application of the rich cosmic muon data set to alignment work. First, a systematic study of cosmic ray and x-ray relative local strip position offsets should be performed for all quadruplets built for the NSWs. The correlation plots such as those presented in Figure 7.2 and 7.3 can reveal unexpected results which could indicate an issue with either cosmic ray or x-ray data collection to be investigated further. Then, the overall correlation between x-ray and cosmic datasets should be quantified for all quadruplets instead of being quantified for each quadruplet individually.

For now, the correlation of the individual quadruplets tested supports the use of the x-ray data to build an alignment model. The plan is that the alignment parameters will be provided to the ATLAS experiment's offline software to estimate the position of each strip and so improve precision muon tracks reconstruction using the sTGCs. Work on the alignment model is ongoing [8]. Currently, the algorithm compares the offsets of a local group of strips at each x-ray gun position as measured by the x-ray and CMM methods in a fit to extract a global slope (m) and offset (b) per layer, i , where the χ^2 is given by Equation 7.1.

$$\chi^2 = \frac{[dy_{cmm,corr} - dy_{xray}]^2}{\delta dy_{xray}^2 + \delta dy_{cmm,corr}^2}, \quad (7.1)$$

$$dy_{cmm,corr} = y_{cmm} + b_i + m_i x - y_{nom} \quad (7.2)$$

Here, dy is a local strip position offset as calculated from the x-ray and corrected CMM data and δdy refers to their respective uncertainties. The large uncertainty on the x-ray local offsets (120 μm) and the sparseness of the measurements means that including input

from other characterization datasets could reduce the uncertainty on the alignment model parameters.

Work on adding the relative local strip position offsets measured using cosmic ray data to the alignment model has begun. They provide alignment information between the x-ray measurement points and can be calculated with a precision relevant to alignment studies. Therefore, they provide additional and complementary information that could further constrain the global rotation and translation parameter of the simple misalignment model currently being used. It is compelling to imagine improving the accuracy of the alignment model given that the accuracy to which the positions of the strips are known in ATLAS will affect the quality of the reconstructed muon tracks used to study high energy physics processes.

Chapter 8

Summary and outlook

The LHC [1] will be at the energy frontier of particle physics for at least the next decade, making it a unique tool with which to study particle physics. With the HL-LHC [2], high statistics on rare particle physics processes will enable more precise measurements of parameters of the Standard Model and increase the sensitivity to signatures of physics beyond the Standard Model [3]. To capitalize on the increased luminosity, the muon small wheels of the ATLAS experiment must be replaced to keep the current triggering and tracking performance [5].

sTGCs are gas ionization chambers optimized for a high rate environment [5]. Using the pad electrodes to define a region of interest makes it possible to get track segments of ~ 1 mrad angular resolution quickly, which will be used as input to check if a collision originated from the interaction point and whether it should be triggered on [5, 53]. Thanks to the careful design of the sTGCs, particularly the small pitch of the strip readout electrodes, the sTGCs are able to provide better than $100 \mu\text{m}$ position resolution per detector plane to fulfill precision offline tracking requirements [6].

Ultimately, the positions of the sTGC strip electrodes need to be known in ATLAS to within $\sim 100 \mu\text{m}$ so that they can deliver the required position resolution [5]. The strategy is to build an alignment model to estimate the position of each strip [8]. Input to the alignment model comes from the datasets used to characterize the quadruplets. The x-ray data [8] is the only characterization dataset that directly links the position of the strips to the ATLAS coordinate system. The alignment model could be built on x-ray data alone, but the sparseness of and large uncertainty on the local offsets mean that the alignment model could benefit from more input. The x-ray method is also a new technique that should be independently validated.

Relative local offsets measured with the cosmics and x-ray datasets were compared and the observed correlation confirmed the local offsets measured with the x-ray gun. Moreover, the

cosmics relative local offsets are useful on their own. The 2D visualizations of relative local offsets make it possible to quickly identify areas of misaligned strips and make hypotheses as to the physical origin of those misalignments. Also, the cosmics residual means were shown to be robust and have uncertainties under 100 μm for all two-fixed-layer reference frames, which is small in this context. Therefore, the cosmics relative local offsets complement the x-ray data by providing a complete, robust picture of the relative strip position offsets between layers. The next goal will be to use the cosmics relative local offsets to improve the alignment model and better position the sTGC strips in ATLAS.

Muons are important signatures of electroweak and Higgs sector events that physicists anticipate studying with a high-statistics dataset [3, 5]. An effective alignment model of sTGC strip positions will ensure that the NSWs can be used to accomplish the ATLAS collaboration’s physics goals during the High Luminosity era of the LHC.

References

- [1] L. Evans and P. Bryant. LHC Machine. *Journal of Instrumentation*, 3(S08001), August 2008.
- [2] G. Apollinari et al. High-Luminosity Large Hadron Collider (HL-LHC) Technical Design Report V. 0.1. Technical Design Report CERN-2017-007-M, CERN, Geneva, Switzerland, September 2017.
- [3] A. Dainese et al. The physics potential of HL-LHC. In *Input to the European Particle Physics Strategy Update*, November 2018.
- [4] ATLAS Collaboration. The ATLAS Experiment at the CERN Large Hadron Collider. *Journal of Instrumentation*, 3(08):S08003, August 2008.
- [5] T. Kawamoto et al. New Small Wheel Technical Design Report. Technical Design Report CERN-LHCC-2013-006, ATLAS-TDR-020, CERN, Geneva, Switzerland, June 2013.
- [6] A. Abusleme et al. Performance of a Full-Size Small-Strip Thin Gap Chamber Prototype for the ATLAS New Small Wheel Muon Upgrade. *Nuclear Instruments and Methods in Physics Research Section A: Accelerators, Spectrometers, Detectors and Associated Equipment*, 817:85–92, May 2016. arXiv: 1509.06329.
- [7] E.M. Carlson. *Results of the 2018 ATLAS sTGC test beam and internal strip alignment of sTGC detectors*. M.Sc. thesis, University of Victoria, Victoria, Canada, 2019.
- [8] B. Lefebvre. Precision survey of the readout strips of small-strip Thin Gap Chambers using X-rays for the muon spectrometer upgrade of the ATLAS experiment. *Journal of Instrumentation*, 15(07):C07013–C07013, July 2020.
- [9] D.J. Griffiths. *Introduction to elementary particles*. Physics textbook. Wiley-VCH, Weinheim, Germany, 2., rev. ed., 5. reprint edition, 2011.

- [10] M.E. Peskin and D.V. Schroeder. *An introduction to quantum field theory*. Addison-Wesley Pub. Co, Reading, Massachusetts, 1995.
- [11] P.A. Zyla et al. Review of Particle Physics. *PTEP*, 2020(8):083C01, 2020.
- [12] M. Kobayashi and T. Maskawa. CP-violation in the renormalizable theory of weak interaction. *Progress of theoretical physics*, 49(2):652–657, February 1973.
- [13] M.L. Perl et al. Evidence for Anomalous Lepton Production in $e^+ — e^-$ Annihilation. *Physical Review Letters*, 35(22):1489–1492, December 1975. Publisher: American Physical Society.
- [14] F. Englert and R. Brout. Broken Symmetry and the Mass of Gauge Vector Mesons. *Physical Review Letters*, 13(9):321–323, August 1964. Publisher: American Physical Society.
- [15] P.W. Higgs. Broken symmetries, massless particles and gauge fields. *Physics Letters*, 12(2):132–133, September 1964.
- [16] D. Galbraith and C. Burgard. UX: Standard Model of the Standard Model, November 2013. <http://davidgalbraith.org/portfolio/ux-standard-model-of-the-standard-model/> last accessed on 2021-09-30.
- [17] C.A. Bertulani. *Nuclear physics in a nutshell*. In a nutshell. Princeton University Press, Princeton, N.J, 2007. OCLC: ocm85690422.
- [18] B.W. Carroll and D.A. Ostlie. *An introduction to modern astrophysics*. Pearson Addison-Wesley, San Francisco, 2nd ed edition, 2007. OCLC: ocm69020924.
- [19] M. Boezio and E. Mocchiutti. Chemical composition of galactic cosmic rays with space experiments. *Astroparticle Physics*, 39-40:95–108, December 2012.
- [20] The SNO Collaboration. Combined analysis of all three phases of solar neutrino data from the sudbury neutrino observatory. *Phys. Rev. C*, 88:025501, August 2013.
- [21] B. Pontecorvo. Neutrino Experiments and the Problem of Conservation of Leptonic Charge. *Soviet Physics—JETP*, 53:1717–1725, 1967.
- [22] S.M. Bilenky and S.T. Petcov. Massive neutrinos and neutrino oscillations. *Reviews of Modern Physics*, 59(3):671–754, July 1987.
- [23] B. Young. A survey of dark matter and related topics in cosmology. *Frontiers of Physics*, 12(2):121201, April 2017.

- [24] C. Muñoz. Dark matter detection in the light of recent experimental results. *International Journal of Modern Physics A*, 19(19):3093–3169, July 2004.
- [25] G. Arnison et al. Experimental observation of isolated large transverse energy electrons with associated missing energy at $s=540$ GeV. *Physics Letters B*, 122(1):103–116, February 1983.
- [26] M. Banner et al. Observation of single isolated electrons of high transverse momentum in events with missing transverse energy at the CERN pp collider. *Physics Letters B*, 122(5):476–485, March 1983.
- [27] G. Arnison et al. Experimental observation of lepton pairs of invariant mass around 95 GeV/c^2 at the CERN SPS collider. *Physics Letters B*, 126(5):398–410, July 1983.
- [28] P. Bagnaia et al. Evidence for $Z \rightarrow e^+e^-$ at the CERN pp collider. *Physics Letters B*, 129(1):130–140, 1983.
- [29] The CDF Collaboration. Observation of Top Quark Production in $\bar{p}p$ Collisions with the Collider Detector at Fermilab. *Physical Review Letters*, 74(14):2626–2631, April 1995. Publisher: American Physical Society.
- [30] The D0 Collaboration. Observation of the Top Quark. *Physical Review Letters*, 74(14):2632–2637, April 1995. Publisher: American Physical Society.
- [31] ATLAS Collaboration. Observation of a new particle in the search for the Standard Model Higgs boson with the ATLAS detector at the LHC. *Physics Letters B*, 716(1):1–29, September 2012. arXiv: 1207.7214.
- [32] The CMS Collaboration. Observation of a new boson at a mass of 125 GeV with the CMS experiment at the LHC. *Physics Letters B*, 716(1):30–61, September 2012. arXiv: 1207.7235.
- [33] Standard Model Summary Plots June 2021, June 2021. <https://atlas.web.cern.ch/Atlas/GROUPS/PHYSICS/PUBNOTES/ATL-PHYS-PUB-2021-032/> last accessed on 2021-09-30.
- [34] O.S. Brüning et al. LHC Design Report. Design Report CERN-2004-003-V-1, CERN, CERN, Geneva, Switzerland, 2004. ISBN: 9789290832249.
- [35] ATLAS luminosity public results run-1, March 2011. <https://twiki.cern.ch/twiki/bin/view/AtlasPublic/LuminosityPublicResults> last accessed on 2021-09-20.

- [36] ATLAS luminosity public results run-2, July 2015. <https://twiki.cern.ch/twiki/bin/view/AtlasPublic/LuminosityPublicResultsRun2> last accessed on 2021-09-20.
- [37] The European Strategy for Particle Physics, 2006. Adopted by the CERN council at a special session at ministerial level in Lisbon in 2006. <http://council-strategygroup.web.cern.ch/council-strategygroup/> last accessed 2021-10-15.
- [38] HiLumi HL-LHC Project. LHC/HL-LHC plan (last update january 2021). <https://hilumilhc.web.cern.ch/content/hl-lhc-project>, last accessed on 2021-09-09.
- [39] M. Cepeda et al. Report from Working Group 2: Higgs Physics at the HL-LHC and HE-LHC. In A. Dainese et al., editors, *Report on the Physics at the HL-LHC, and Perspectives for the HE-LHC*, number CERN-LPCC-2018-04, pages 221–584. 364 p, CERN, Geneva, Switzerland, Jun 2018. CERN.
- [40] ATLAS Inner Detector Community. ATLAS inner detector : Technical Design Report, 1. Technical Design Report CERN-LHCC-97-016, CERN, Geneva, Switzerland, April 1997. ISBN: 9789290831020 Publication Title: CERN Document Server.
- [41] S. Haywood, L. Rossi, R. Nickerson, and A. Romanouk. ATLAS inner detector : Technical Design Report, 2. Technical Design Report CERN-LHCC-97-017, CERN, Geneva, Switzerland, April 1997. ISBN: 9789290831037 Publication Title: CERN Document Server.
- [42] C. Grupen, B.A. Shwartz, and H. Spieler. *Particle detectors*. Cambridge University Press, Cambridge, UK; New York, 2008. OCLC: 1105536566.
- [43] ATLAS LARG Unit. ATLAS liquid-argon calorimeter : Technical Design Report. Technical Design Report CERN-LHCC-96-041, CERN, Geneva, Switzerland, December 1996. ISBN: 9789290830900 Publication Title: CERN Document Server.
- [44] ATLAS Collaboration. ATLAS tile calorimeter : Technical Design Report. Technical Design Report CERN-LHCC-96-042, CERN, Geneva, Switzerland, 1996. ISBN: 9789290830917 Publication Title: CERN Document Server.
- [45] ATLAS Level-1 Trigger Group. ATLAS level-1 trigger : Technical Design Report. Technical Design Report CERN-LHCC-98-014, CERN, Geneva, Switzerland, August 1998. ISBN: 9789290831280 Publication Title: CERN Document Server.
- [46] ATLAS Collaboration. Technical Design Report for the Phase-II Upgrade of the ATLAS TDAQ System. Technical Design Report CERN-LHCC-2017-020, ATLAS-TDR-029, CERN, Geneva, Switzerland, September 2017.

- [47] A. Ruiz Martínez. The run-2 ATLAS trigger system. *Journal of Physics: Conference Series*, 762:012003, October 2016.
- [48] P. Jenni, M. Nessi, M. Nordberg, and K. Smith. ATLAS high-level trigger, data-acquisition and controls : Technical Design Report. Technical Design Report CERN-LHCC-2003-022, CERN, Geneva, Switzerland, July 2003. ISBN: 9789290831280 Publication Title: CERN Document Server.
- [49] ATLAS Muon Collaboration. ATLAS Muon Spectrometer: Technical Design Report. Technical Design Report CERN-LHCC-97-022, CERN, Geneva, Switzerland, June 1997.
- [50] ATLAS/Magnet Project Collaboration/Cern-ATLAS Team. ATLAS magnet system : Technical Design Report, 1. Technical Design Report CERN-LHCC-97-018, CERN, Geneva, Switzerland, April 1997. ISBN: 9789290831044 Publication Title: CERN Document Server.
- [51] ATLAS Collaboration. Performance of the ATLAS muon trigger in pp collisions at $\sqrt{s} = 8$ TeV. *The European Physical Journal C*, 75(3):120, March 2015. arXiv: 1408.3179.
- [52] S. Aefsky et al. The Optical Alignment System of the ATLAS Muon Spectrometer End-caps. *Journal of Instrumentation*, 3(11):P11005–P11005, November 2008. Publisher: IOP Publishing.
- [53] E. Perez Codina. Small-strip Thin Gap Chambers for the muon spectrometer upgrade of the ATLAS experiment. *Nuclear Instruments and Methods in Physics Research Section A: Accelerators, Spectrometers, Detectors and Associated Equipment*, 824:559–561, July 2016.
- [54] J. Townsend. *Electricity in gases*. Clarendon Press, Oxford, 1915.
- [55] S. Majewski, G. Charpak, A. Breskin, and G. Mikenberg. A thin multiwire chamber operating in the high multiplication mode. *Nuclear Instruments and Methods*, 217:265–271, 1983.
- [56] E. Gatti, A. Longoni, H. Okuno, and P. Semenza. Optimum geometry for strip cathodes or grids in MWPC for avalanche localization along the anode wires. *Nuclear Instruments and Methods*, 163(1):83–92, July 1979.
- [57] G. Battistoni et al. Resistive cathode transparency. *Nuclear Instruments and Methods in Physics Research*, 202(3):459–464, November 1982.

- [58] B. Lefebvre. *Characterization studies of small-strip Thin Gap Chambers for the ATLAS Upgrade*. PhD thesis, McGill University, Montreal, Canada, 2018.
- [59] P.K.F. Grieder. *Cosmic rays at Earth: researcher's reference manual and data book*. Elsevier Science Ltd, Amsterdam, 1st ed edition, 2001.
- [60] R. Keyes et al. Development and characterization of a gas system and its associated slow-control system for an ATLAS small-strip thin gap chamber testing facility. *Journal of Instrumentation*, 12(04):P04027–P04027, April 2017.
- [61] G. Iakovidis. VMM3, an ASIC for Micropattern Detectors. In *5th International Conference on Micro-Pattern Gas Detectors (MPGD2017)*, number ATL-MUON-PROC-2018-003 in Proceedings of Science, March 2018.
- [62] B. Chen. *Calibration Studies of the Front-End Electronics for the ATLAS New Small Wheel Project*. M.Sc. thesis, McGill University, Montreal, Canada, 2019.
- [63] R. Brun and F. Rademakers. ROOT: An object oriented data analysis framework. *Nuclear Instruments and Methods in Physics Research Section A: Accelerators, Spectrometers, Detectors and Associated Equipment*, 389:81–86, 1997. See also "ROOT" [software], Release 6.18/02, 23/08/2019, (<https://zenodo.org/record/3895860#.YVJW6n0pCHs>).
- [64] F. Sauli. Principles of operation of multiwire proportional and drift chambers. Number 81 in CERN Academic Training Lectures, CERN, Geneva, Switzerland, September 1975 – June 1976. CERN.
- [65] M. Hatlo et al. Developments of mathematical software libraries for the LHC experiments. *IEEE Transactions on Nuclear Science*, 52:2818–2822, 2005.
- [66] H. Guo. A Simple Algorithm for Fitting a Gaussian Function [DSP Tips and Tricks]. *IEEE Signal Processing Magazine*, 28(5):134–137, September 2011.
- [67] I. Endo et al. Systematic shifts of evaluated charge centroid for the cathode read-out multiwire proportional chamber. *Nuclear Instruments and Methods in Physics Research*, 188(1):51–58, September 1981.
- [68] Minature x-ray source mini-x. Product of Amptek Inc. <https://www.amptek.com/-/media/ametekamptek/documents/resources/specs/mini-x-specifications.pdf?la=en&revision=512f7eb3-01b3-47fd-864f-5525c850fc6e&hash=B8B03C0592486E2D91C566C4326F15F5>, last accessed on 2021-10-15.

- [69] B. Stelzer. The New Small Wheel Upgrade Project of the ATLAS Experiment. *Nuclear and Particle Physics Proceedings*, 273-275:1160–1165, April 2016.
- [70] X. Zhao et al. Cosmic test of sTGC detector prototype made in China for ATLAS experiment upgrade. *Nuclear Instruments and Methods in Physics Research Section A: Accelerators, Spectrometers, Detectors and Associated Equipment*, 927:257–261, May 2019.

APPENDICES

Appendix A

Uncertainty in cluster positions

Cluster centroids are better modeled by a Gaussian fit than a simple weighted mean because the Gaussian tails better take into account the charge deposited on the outer strips. Also, the Gaussian fit is less biased by differential non-linearity [58].

No uncertainty on the peak signal amplitudes of a cluster are assigned since clusters are not built from samples of a Gaussian distribution but instead are digitized measurements of signal amplitude versus position.

The clusters were fit with Guo's method [66] and Minuit2 for ROOT [65]. Guo's method is an analytic solution that takes into account noise, which is good for computational scalability. Minuit2 is the standard fitting algorithm used in particle physics at ATLAS. The difference in cluster means between the two algorithms for all clusters recorded on a given quadruplet is shown in Figure A.1.

The difference in cluster means calculated with each algorithm is centered around zero indicating that the two algorithms are not biased with respect to one another. The RMS of the distribution in Figure A.1 is 57 μm , which is much larger than the statistical uncertainty in the mean calculated by the Minuit2 algorithm, which peaks around 7 μm . There is no reason to suspect that one algorithm calculates a more accurate mean than the other, so the uncertainty in the cluster mean should account for the variation between algorithms. An RMS of 60 μm was common for data taken with a sample of quadruplets at 3.1 kV. Therefore, a conservative estimate of the uncertainty in the reconstructed cluster y -coordinate is 60 μm .

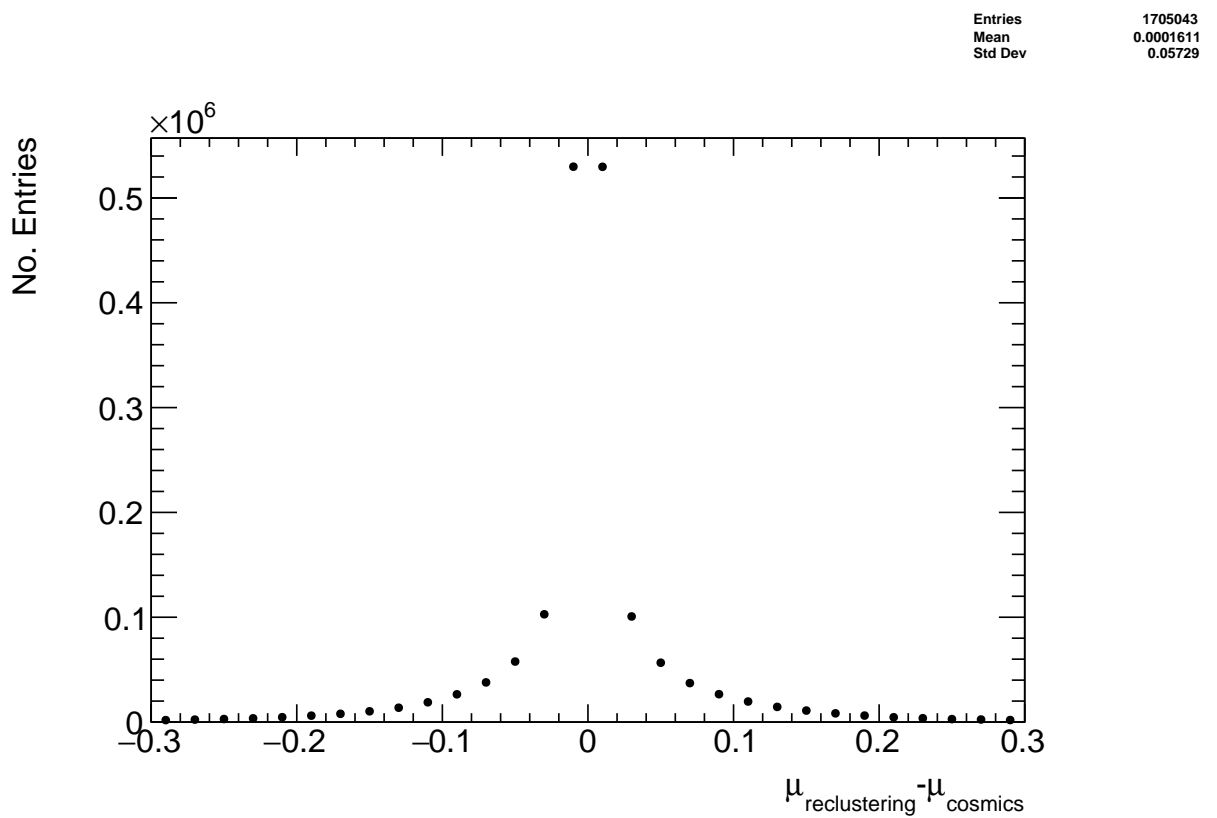


Figure A.1: The difference between cluster means calculated with Guo's method [66] and Minuit2 for ROOT [65] for data collected with QL2.P.8 at 3.1 kV.

Appendix B

Study of cosmics for alignment analysis statistical uncertainty

Typically, one million triggers (cosmic muon events, noise, photons and δ -rays) were collected for each Canadian quadruplet at McGill University, resulting in roughly half the number of viable tracks after cuts. For QS3.P.18, 3.5 million triggers were collected. To gauge the sensitivity of the analysis to the available statistics, partitions of this data with each with a different number of triggers were analyzed separately. Ultimately, the quantity of interest was the Gaussian mean of the residual distribution in regions of interest, so the peak in the distribution of the statistical uncertainty in the residual means for each area of interest for a specific tracking combination was used to gauge the quality of the analysis. How the peak in the residual mean uncertainty distribution changes with the number of triggers is shown in Figure B.1 for tracks on layer 1 built from layers 3 and 4.

The uncertainty is already around $20\text{ }\mu\text{m}$ at 1 million triggers, suitable for distinguishing differences in relative local offsets of order $50\text{ }\mu\text{m}$ as required. Although collecting more triggers could decrease the statistical uncertainty, it is not required for the goals of this analysis. Moreover, the systematic uncertainty on the mean cosmics residuals is around $50\text{ }\mu\text{m}$ so the statistical uncertainty of $20\text{ }\mu\text{m}$ is nearly negligible.

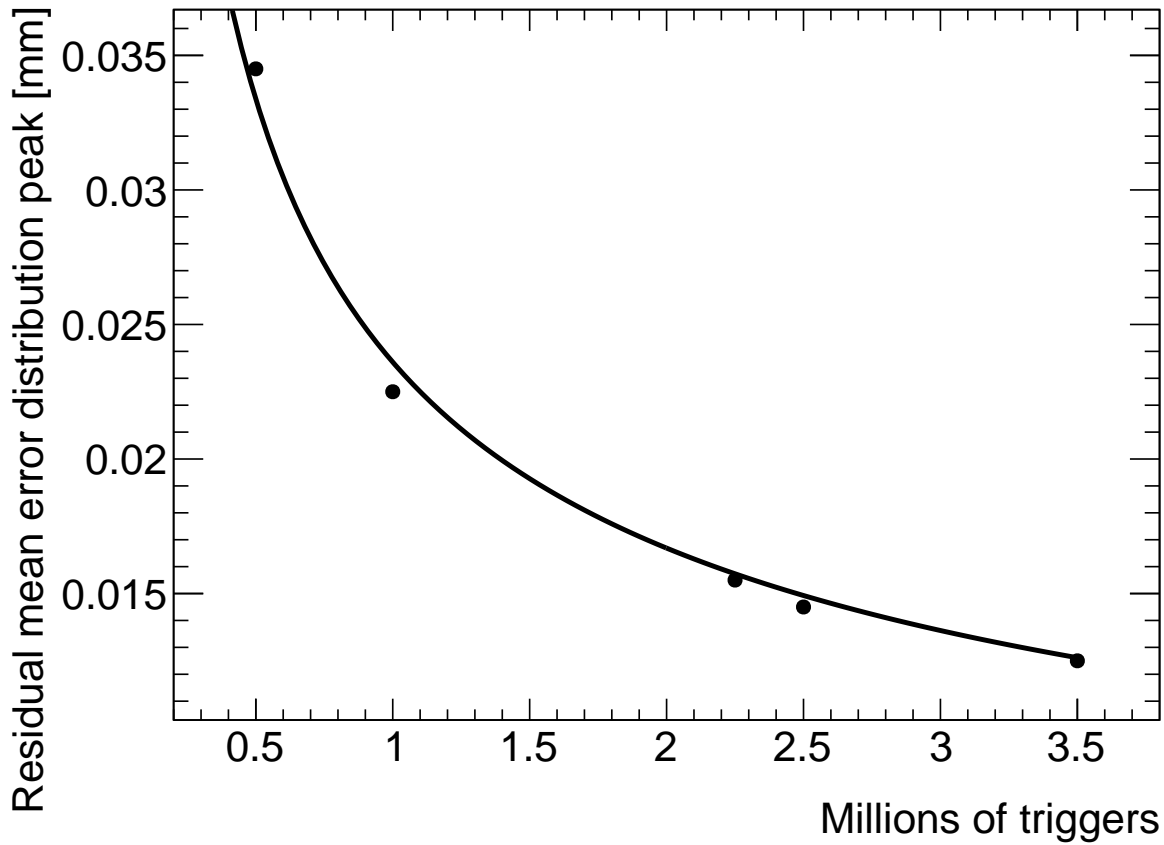


Figure B.1: How the peak of the distributions of uncertainties in the residual means in regions of interest for tracks on layer 1 built from layers 3 and 4 changed with the number of triggers used in the analysis. The black line is a fit to $\frac{C}{\sqrt{N}}$, where N is the number of triggers and C is a constant. The distribution falls off proportionally to $\frac{1}{\sqrt{N}}$ as expected.

Appendix C

Study of systematic uncertainties when using cosmics data for alignment studies

C.1 Residual distribution fit function

The distribution of residuals should be modeled by a double Gaussian fit[58]:

$$G(r) = A_s \exp\left[\frac{-(r - \mu)^2}{2\sigma_s^2}\right] + A_b \exp\left[\frac{-(r - \mu)^2}{2\sigma_b^2}\right] \quad (\text{C.1})$$

where r is the residual, A is the Gaussian amplitude, μ is the Gaussian mean, σ is the Gaussian sigma, and the subscripts s and b stand for signal and background respectively. One Gaussian captures the real (signal) tracks and the other captures the tracks built from noise (background). The Gaussian with the smaller width is identified as the signal.

A double Gaussian fit was more prone to failure than a single Gaussian fit. The Gaussian fits were performed by initially estimating the amplitude to be 100 tracks, the Gaussian mean to be the histogram mean, and Gaussian σ to be the RMS. The fit range was restricted to ± 1 root-mean-square (RMS) from the histogram mean. The modification helped the Gaussian fit capture the signal peak. An example residual distribution is shown in Figure C.1.

For all residual distributions in 100 mm by 100 mm bins on layer 4 built from clusters on layers 1 and 2, the difference in Gaussian and double Gaussian means and σ 's is shown in Figure C.2a. The mean of the distribution is centered around zero (within the RMS of the

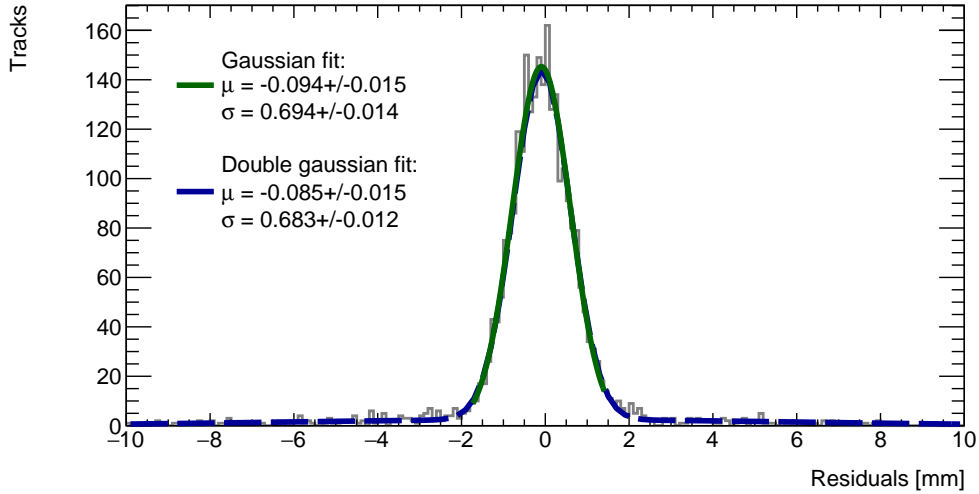
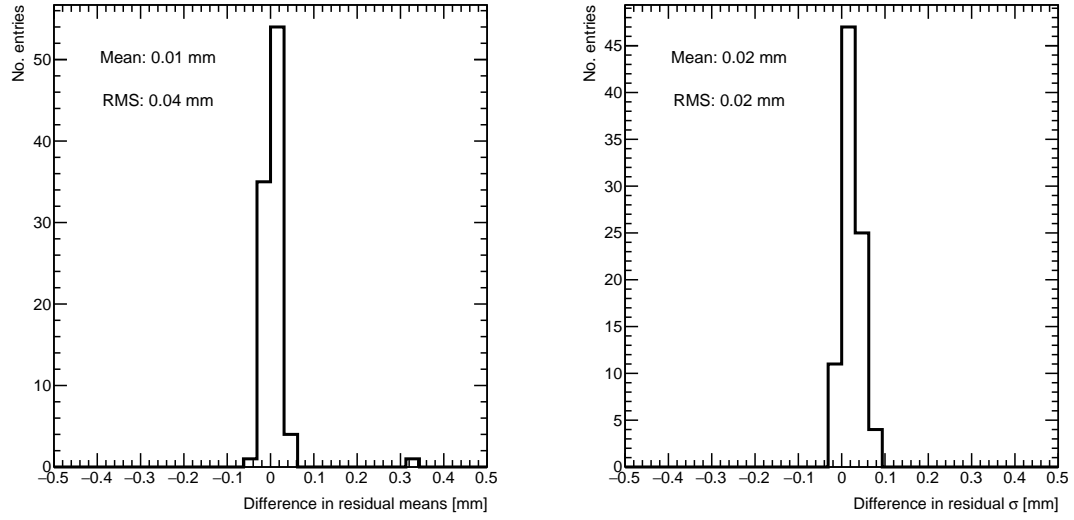


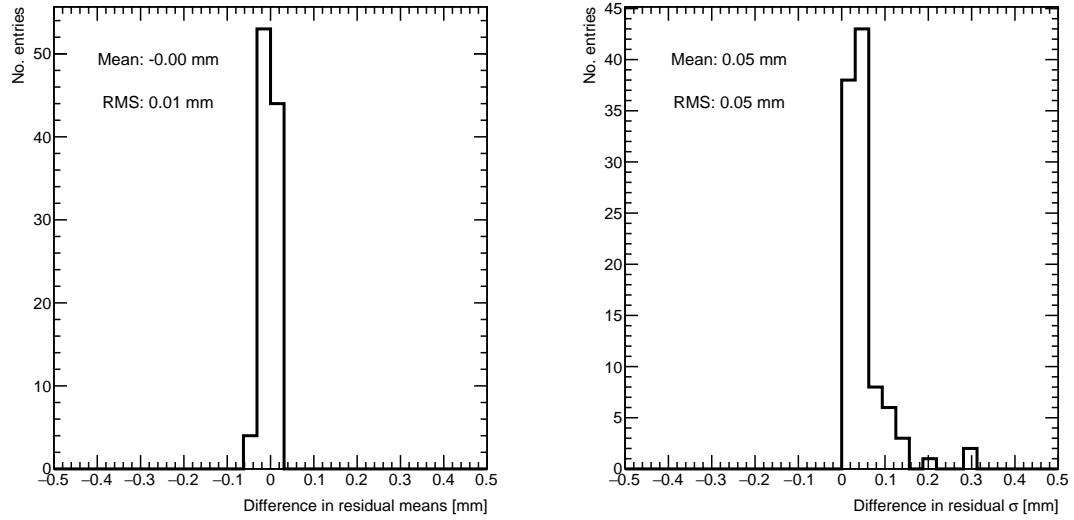
Figure C.1: Residual distribution for track residuals on layer 4 built from clusters on layers 1 and 2 for $x \in [-3.00, 97.00]$ mm, $y \in [394.60, 494.60]$ mm, fit with a double Gaussian and a single Gaussian in a range of ± 1 RMS from the histogram mean.

distribution) so the choice of fit algorithm imbues no measurable bias. The order of the RMS is such that the difference in residual means at 40 μm is just significant, so it should be accounted for as a systematic uncertainty on the Gaussian residual means. The 40 μm RMS is for the tracking combination with the worst extrapolation lever arm and the widest distribution of mean differences; the interpolation combinations have narrower distributions, as shown in Figure C.2b. The RMS of the distribution for residual means on layer 2 obtained using reference layers 1 and 3 is only 10 μm , which is almost negligible.

The Gaussian σ should be larger than the double Gaussian σ because the Gaussian distribution includes the effect of the noise tracks that can yield large residuals, while the double Gaussian models signal and background residuals separately. For this analysis, only the residual mean was important, so the systematic overestimate of the signal σ in the Gaussian fit shown in the right-side plots of Figure C.2 was allowed.



(a) Difference in residual distribution means (left) and σ 's (right) extracted with a Gaussian and double Gaussian fit, for all residual distributions in 100 mm by 100 mm bins on layer 4 built from clusters on layers 1 and 2 for sample quadruplet QL2.P.8.



(b) Difference in residual distribution means (left) and σ 's (right) for a Gaussian and double Gaussian fit, for all residual distributions in 100 mm by 100 mm bins on layer 2 built from clusters on layers 1 and 3 for sample quadruplet QL2.P.8.

Figure C.2

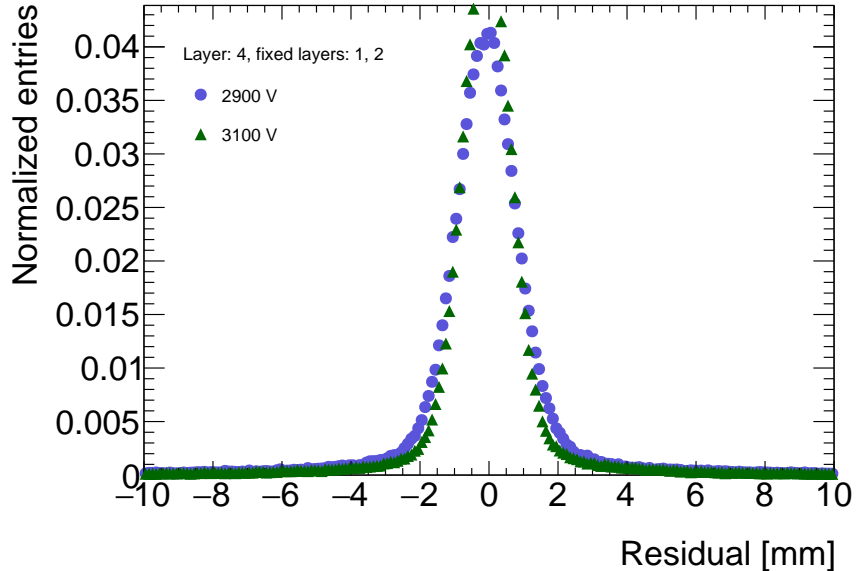


Figure C.3: Residual distribution for tracks on layer 4 built from clusters on layers 1 and 2 for sample quadruplet QL2.P.8 for data collected at 2.9 kV and 3.1 kV.

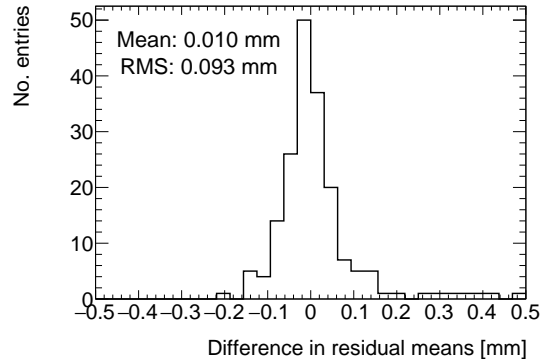
Ultimately, a Gaussian fit was chosen for the track residual distributions because it was more robust and there was little significance in the difference between the residual means calculated with either algorithm.

C.2 Cosmic muon data collection voltage

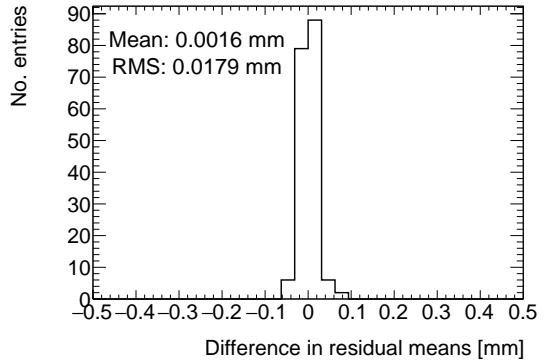
Cosmic muon data was collected at 2.9 kV and 3.1 kV because although 2.9 kV is closer to the operating conditions the chambers will be subject to in ATLAS, the extra gain provided by operating at 3.1 kV increased the signal to noise ratio for pad signals. Also, the tracking efficiency was higher with data collected at 3.1 kV. As such, cosmic muon data collected at 3.1 kV was used in the analysis presented in the body of the thesis.

The difference in gain affects the relative population of clusters of different sizes, which in turn affects the uncertainty in the mean cluster positions on each layer, the uncertainty in the track positions and the residual distributions. The residual distributions for 3.1 kV data are narrower, as shown in Figure C.3.

Neither dataset is better for calculating the mean of residuals in a given area, so a systematic uncertainty can be assigned based on the difference in residual means calculated for 2.9 kV



(a) Difference in residual means for residuals on layer 4 built from clusters on layers 1 and 2.



(b) Difference in residual means for residuals on layer 2 built from clusters on layers 1 and 3.

Figure C.4: Difference in residual means for data collected with sample quadruplet QL2.P.8 at 2.9 kV and 3.1 kV respectively in 100 mm by 100 mm bins.

and 3.1 kV data per tracking combination. For each tracking combination, the difference in the fitted track residual means in 100 mm by 100 mm areas for 2.9 kV and 3.1 kV data are put in a distribution for a sample quadruplet, as shown in Figure C.4. The means of the distributions for both tracking combinations are near zero, so as expected the collection voltage introduces no bias. Tracks built from clusters on layers 1 and 2 and extrapolated to layer 4 have the worst lever arm and hence the largest root-mean-square (RMS) of 100 μm . The width of the distributions for geometrically favourable tracking combinations are much narrower. The narrowest width of the residual mean difference distribution is for tracks on layer 2 built from clusters on layers 1 and 3 (see Figure C.4b), with a value of 20 μm .

C.3 Cluster fit algorithm

To ensure that changing the cluster fitting algorithm like in Appendix A would not change the calculated mean of residuals in each region of interest significantly, the residual means were compared in both cases. The distribution of the difference in residual means is plotted in Figure C.5 for the tracking combinations with the worst and most favourable extrapolation lever arms.

The mean of the distributions are centered around zero, so the choice of cluster fit algorithm did not introduce any bias. Differences on the order of 50 μm are important, so the root-mean-squares (RMS's) of the distributions show that the clustering algorithm had a small

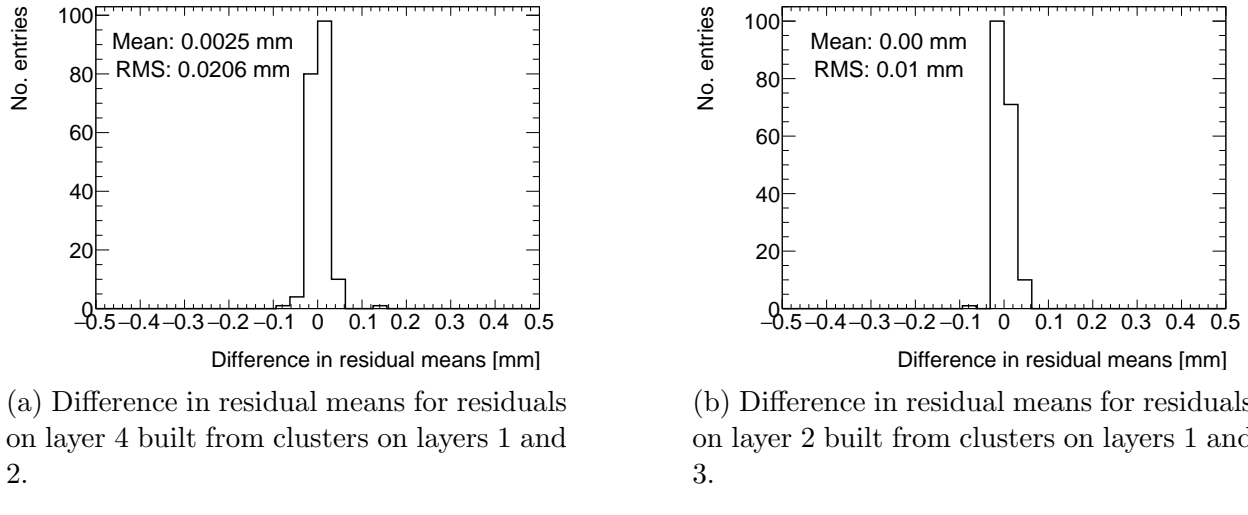


Figure C.5: Difference in residual means when the cluster fit algorithm is `Minuit2` [65] versus Guo’s method [66] for two different tracking combinations for sample quadruplet, QL2.P.8.

but notable effect between 10-20 μm from the most to least geometrically favourable tracking combinations. Therefore, the RMS for each tracking combination will be used to add a systematic uncertainty on the residual means accounting for the effect that different cluster fit algorithms have on the residual means.

C.4 Differential non-linearity

Definition

In this context, differential non-linearity (DNL) is when the reconstructed cluster mean is biased by the fit of the discretely sampled peak signal amplitude distribution over the strips. The bias depends on the relative position of the avalanche with respect to the center of the closest strip. For a summary of DNL, refer to page 40 of [58], an early paper studying its effects [67], and for an example application, refer to [6].

Application and effect of DNL

The cluster mean was corrected for DNL using the equation:

$$y' = y + a \sin(2\pi y_{rel}) \quad (\text{C.2})$$

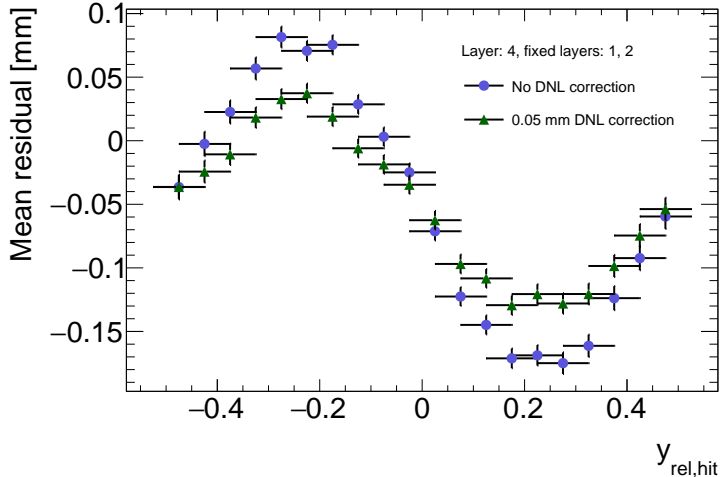


Figure C.6: Effect applying a $50\text{ }\mu\text{m}$ DNL correction to the profile of the residuals sorted by y_{rel} for residuals built from clusters on layers 1 and 2 and extrapolated to layer 4 of quadruplet, QL2.P.8.

where y is the cluster mean, y_{rel} is the relative position of the cluster mean with respect to the strip's center, a is the amplitude of the correction, and y' is the corrected cluster mean. The amplitude can be derived by comparing the reconstructed hit position to the expected hit position, as done in [6]. With cosmic muons, there is no reference hit position to compare to, so track residuals were used as a proxy [58]. The hallmark of the DNL effect is the periodic pattern in the residual versus y_{rel} profile, and the effect of correcting the cluster means using an amplitude of $50\text{ }\mu\text{m}$ is shown in Figure C.6. An amplitude of $50\text{ }\mu\text{m}$ is based on Dr. Lefebvre's [58] estimate of the DNL amplitudes by layer, quadruplet and cluster size using cosmic muon tracks [58]. Little variation is seen in the amplitude parameters with respect to the quadruplet tested, the layer and the cluster size so a universal correction is used.

Although the correction is not large enough in this case, the figure shows that the correction does reduce the DNL effect. Slightly better performance is seen in the interpolation tracking combinations where the quality of the residuals is better. DNL corrections for cosmic muon data are difficult because the DNL effect is obscured by the effect of misalignments between strip layers and noise. Misalignments cause the center of the sinusoidal pattern in Figure C.6 to be shifted off of zero, since the mean of residuals is shifted.

Figure C.7 shows the distribution of the difference in residual means calculated in 100 mm by 100 mm areas for mean track residuals on layer 4 obtained using layers 1 and 2 as reference.

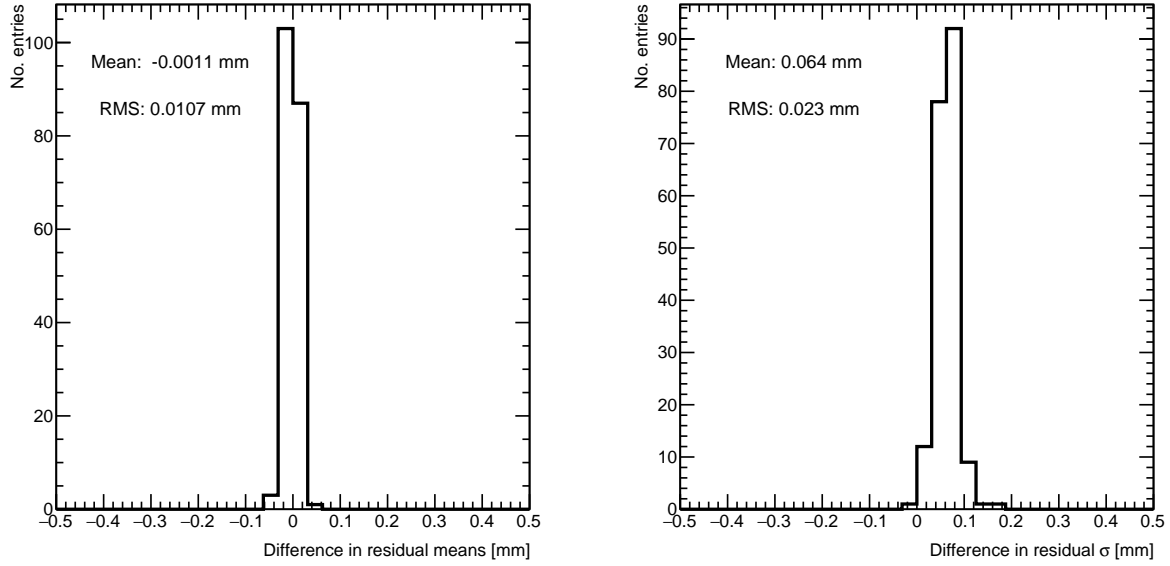


Figure C.7: Difference in residual distribution means and σ 's with and without DNL correction for residuals on layer 4 obtained using reference layers 1 and 2 for sample quadruplet, QL2.P.8.

The mean of the distribution is zero within the root-mean-square so the DNL correction does not bias the residual means. It is apparent that the effect of the DNL correction on the residual means is on the order of micrometers given the RMS of $10\text{ }\mu\text{m}$ in the worst extrapolation case. Although the σ 's of the residual distributions shrink with the DNL correction, the mean is the parameter of interest so the bias in the fitted σ 's was ignored. Therefore, in this analysis DNL is not corrected for.

Appendix D

Printable plots

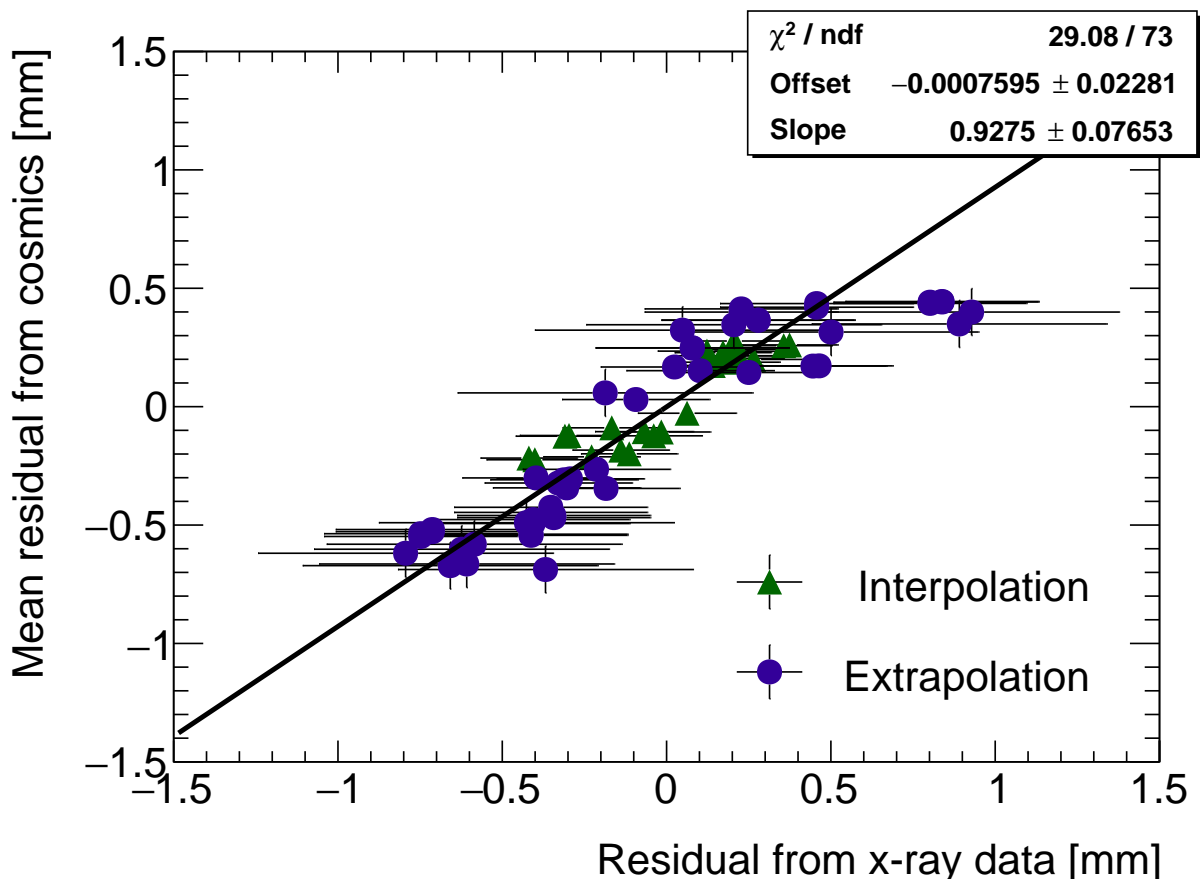


Figure D.1: Correlation plot between x-ray and mean cosmics residuals in 100 mm by 100 mm bins for all tracking combinations for QL2.P.11. This is a printable version of Figure 7.2 in Section 7.1.

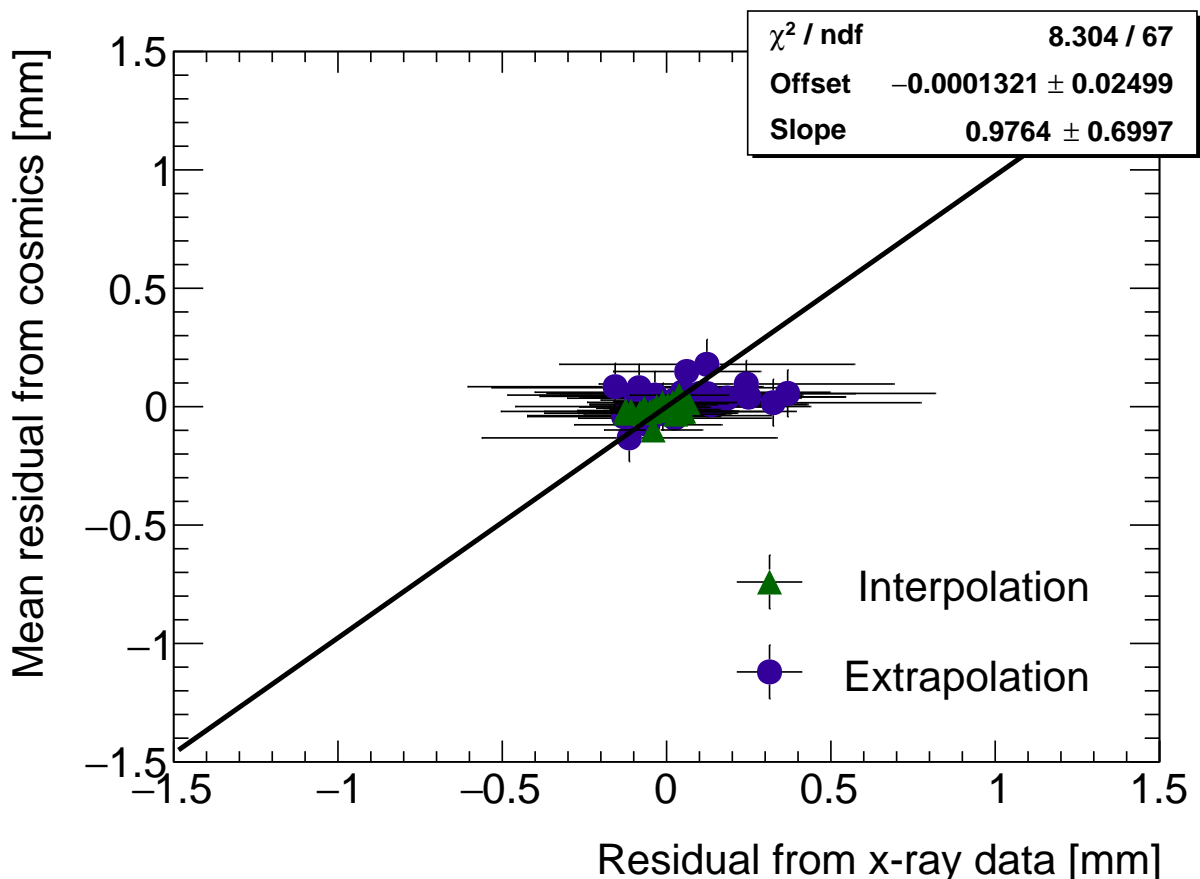


Figure D.2: Correlation plot between x-ray and mean cosmics residuals in 100 mm by 100 mm bins for all tracking combinations for QL2.P.8. This is a printable version of Figure 7.3 in Section 7.1.